Geometry and shape inversion in Choanoeca flexa

Figs/University_Crest.pdf
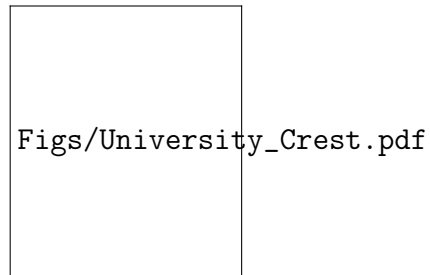
Adam Konkol

Advisor: Dr. R. E. Gold-
stein

Department of Physics
University of Cambridge

This thesis is submitted for the degree of
Master of Philosophy

Churchill College   July 2022

I would like to dedicate this thesis to my loving parents . . .

ak2351: dedicate to people!

Declaration

I hereby declare that except where specific reference is made to the work of others, the contents of this dissertation are original and have not been submitted in whole or in part for consideration for any other degree or qualification in this, or any other university. This thesis is my own work and includes nothing which is the outcome of work done in collaboration except where specifically indicated in the text. This thesis contains fewer than 15,000 words including appendices, bibliography, footnotes, and tables.

<div align="right">

Adam Konkol

July 2022

</div>

Acknowledgements

And I would like to acknowledge ...

ak2351: acknowledge people!

Abstract

The newly discovered multicellular choanoflagellate Choanoeca flexa forms a curved sheet that undergoes a functional, light-triggered inversion. This change in orientation that allows the organism to reversibly switch between efficient swimming and feeding shapes provides an opportunity to study biological exploitation of geometry in an evolutionarily basal context. I sought to model the mechanics that produce this apparent bistability and the dynamics of the active transformation between the two states.

In this work, I approach the modeling problem from complementary continuous and discrete mechanics perspectives. Since radial expansion and contraction at a given latitude require azimuthal stretching and shrinking, a one-dimensional filament model does not capture the energetic barriers encountered by the sheet during the transition. Using energy functional variation, I solve for the forces acting throughout the sheet and derive corresponding equilibrium shape equations. Both views establish that C. flexa inversion can be hindered in sufficiently large sheets by cell collars connecting adjacent cells stretching.

Comparisons between the discrete model for C. flexa mechanics and previously published experimental results support that collar stretching at the edges interferes in sheet inversion. Treating the organism as a crystal lattice defined by cells and cell-cell interactions, we recognise that the graph degree of cells plays a substantial role in overall sheet curvature and ability to invert.

My results suggest that the graph topology of the cell-cell interface network must accommodate inversion, particularly at the edge of the sheet. Future work should image C. flexa flipping and observe changes in connectivity that accompany the transition. My results link graph topology with a notion of surface curvature through established ideas in the theory of crystal structure.

Table of contents

List of figures

List of tables

Nomenclature

boundary cells cells with free collar microvilli

Chapter 1

Introduction

1.1   Background

Discuss evolutionary origins of multicellularity and some basic examples like Volvox. What drives organisms to become multicellular? We expect there was genuine evolutionary favorability to developing multicellularity. In the volvocine algae, it is believed that the transition to multicellularity and cooperation of distinct differentiated cells has occured several times [15]. Across all eukaryotic lineages, there is evidence that multicellularity evolved independently many times [17].

Organisms like vovocine green algae and choanoflagellates are sought as models in the search for evolutionary origins of multicellularity for both their biological and physical features [14]. Choanoflagellates have long been regarded as a close relative to the animal kingdom owing to their similarity to choanocytes in sponges [16], and we now understand them to be most closely related by genetics [20, 29]. These organisms' colonies are also large enough that they operate at high Péclet number ($Pe \sim 10^2$), the ratio between advective and diffusive transport, meaning that advection must contribute substantially to deriving food [31]. This of course contrasts with typical bacteria, where diffusion dominates nutrient transport [3].

1.1.1   Why attach?

> ak2351: could probably say some stuff about bacteria and biofilms here

From a simplistic optimality perspective, we do not readily identify a motivation for attaching. Michelin and Lauga [27] demonstrated that regardless of Péclet number, cells feed optimally when they maximise their swimming velocity. Despite this solution, Kirkegaard

and Goldstein [18] modeled for cell arrangements such as the choanoflagellate colonies to be studied in this work (section 1.2) that swimming is maximised for individual cells. When collared choanoflagellates are near each other, cells with their flagella pointing in the same direction (*i.e.* a straight chain) are best at swimming. Based on feeding efficiency via swimming alone, it does not appear that basic aquatic multicellular colonies, such as *S. rosetta* or *C. flexa* have much to gain from their propulsion cooperation.

The organisms in the *Volvox* genus are well studied for being a primitive example of multicellularity and a shining beacon of functional geometric changes. These organisms attach their cells to one another using an extra-cellular matrix, as *S. rosetta* does as well (discussed later).

One suggestion for cell-cell attachment in colonies is to avoid phagocytosis from predators by physically becoming too large. Stanley [32] argues that the emergence of heterotrophs, or organisms that derive energy by consuming others, led to rapid diversification and the rise of multicellularity through intense selective pressure. Boraas et al. [4] demonstrated in a laboratory culture that stable multicellularity emerged in the green alga *Chlorella vulgaris* when exposed to predators. Eight-cell colonies were observed to predominate, indicating that multicellularity emerged to balance colony survival as well as individual demands of each cell.

Attaching supports generating flows

Spherical colony geometries have long been documented [22] for choanoflagellates.

We understand, for example, in *Volvox* colonies that driving flows supports nutrient transport by advection as well as phototaxis.

ak2351: Here is a good place to describe sponges!

1.1.2   Why differentiate?

We are interested in multicellularity at an evolutionarilty basal level to understand the basic reasons that life evolved to form multicellular organisms. Sponges are as basal as multicellular animal life goes

ak2351: Discuss why and reference a review about sponges evolutionary simplicity. Carr et al. [8] could be a good ref to give here regarding choanoflagellates

.

ak2351: discuss Dayel et al. [9] about differentiation in *S. rosetta*

While we are interested in sponges since they are members of the animal kingdom, choanoflagellates are often considered to be evolutionarily and morphologically comparable.

1.2   Choanoflagellates

ak2351: Discuss Carr et al. [8] about molecular phylogeny of choanoflagellates

The connection between choanoflagellates and animals predates studies using molecular phylogeny. James-Clark [16] first compared choanoflagellate morphology with the choanocytes in sponge choanocyte chamber. Morphological similarities between choanocytes and protists led to the belief that the two emerged from a common ancestor [10, 34].

Mah et al. [26] offers the first comprehensive comparison between sponge choanocyte and choanoflagellate morphology. Sponge collars are fairly cylindrical while choanoflagellate collars are more cone-like. Choanoflagellates have glycocalyx, but seemingly around the cell body [25]. Notably the collars in choanoflagellates are always microvillar and always present, while in sponges they emerge as a consequence of cell differentiation

ak2351: cite this!

.

Choanoflagellates are increasingly studied as a model for understanding how multicellular animal life emerged. Fairclough et al. [13] shows that the transition from single cell to multicellular colony in *Salpingoeca rosetta* occurs by cell division, with cells remaining attached to each other.

S. rosetta has an extracellular matrix [21]. Larson et al. [21] finds that the extracellular matrix constrains cells to grow and divide to a given colony shape. This paper also finds that *S. rosetta* does not have distinct cell lineages or a developmental plan.

Kirkegaard and Goldstein [18] finds that collared choanoflagellates drive the most flow through their collars by swimming fastest, which occurs in the unicellular state [27]. This makes it unclear that forming rosette colonies is for the sake of improved feeding. The authors point to evidence that *S. rosetta* is induced to form rosette colonies by bacterial cues to suggest that the reasons for the development of multicellularity may be more subtle than previously expected [1].

1.3 *Choanoeca flexa*

Brunet et al. [6] describe a newly discovered choanoflagellate, *Choanoeca flexa*, which lives and feeds in aquatic environments. Here, I describe the relevant properties and characteristics of these cells and their colonies for modeling its structure and behavior. All descriptions of *C. flexa* proceed from Brunet et al. [6] and private communications with the authors.

C. flexa is an aquatic colonial choanoflagellate that forms sheets on the order of $100\,\mu m$ in diameter (figure 1.2). Each cell in a colony consists of a cell body ($\sim 4\,\mu m$), microvillar collar ($\sim 10\,\mu m$ length), and apical flagellum at the collar centre. All observed sheets have had flagella facing in the same direction, giving the sheet two distinct sides. Cells attach to each other through their collar microvilli, and in contrast to a colonial flagellate like *S. rosetta*, there is no evidence for an extracellular matrix holding cells together in *Choanoeca* [24, 6]. Collar microvilli are distinct and colony cells demonstrated no intercellular cytoplasmic bridges (contrast with *i.e. Volvox*), with cells detaching from each other upon treatment with calcium [5].

ak2351: double check that it was calcium!

By comparison with division in *C. perplexa*, colony cells are expected to undergo cell division with temporary incomplete replication, where the pair of daughter cells is attached by some shared collar microvilli (figure 1.1). Colonies are believed to occasionally fragment to separate completely and multiply [24].

C. flexa also exhibits a sedentary, unicellular form that adheres to surfaces via a stalk (*theca*) without a flagellum, as in *C. perplexa*. Our understanding of cell division in *Choanoeca* emerges from the thecate form, which leaves one thecate daughter cell and another motile, flagellated cell. Division begins with the generation of a flagellum by the thecate cell and proceed with protoplasm division with incomplete separation at collar microvilli (figure 1.1) [12, 23]. The remainder of this work concerns the colonial form of *C. flexa* rather than the thecate or unicellular motile forms. While we do not have observations on cell replication in the colonial phase, *S. rosetta* gives a suggestion that colonial choanoflagellates do not coordinate their cell division [13].

While choanoflagellate colonies typically orient their flagella to point away from the colony centre, sheets of *Choanoeca* in their rest state point flagella inward.

ak2351: cite this! Brunet et al. [6] uses a leadbeater textbook
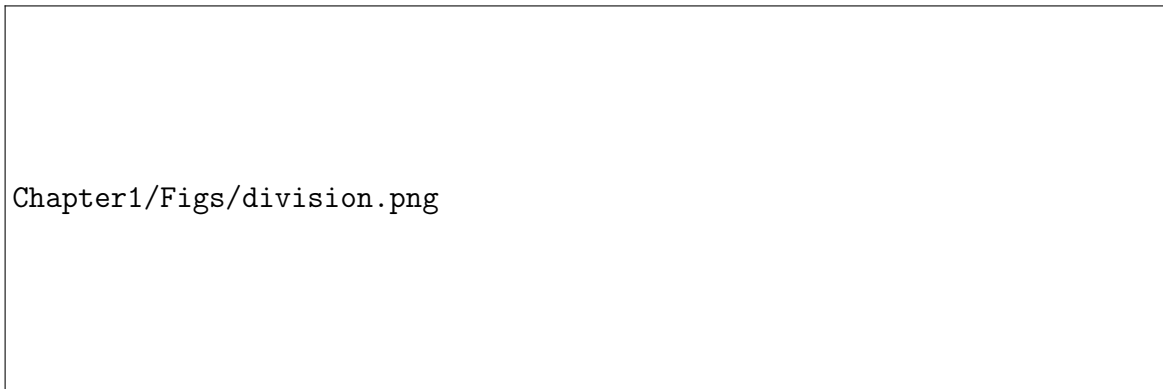
Fig. 1.1 Illustrations of stages of division in the sessile form of *C. perplexa*. Reproduced from Leadbeater [23] based on Ellis [12] with permission from Cambridge University Press.

1.3.1   Sheet inversion

Choanoeca has recently sparked renewed interest as a result of the characterisation of rapid light-regulated inversion in colonies, which causes cell sheets to change orientation from pointing flagella-in to flagella-out [6]. The inversion is understood to result from contraction of an actomyosin ring at the apical end of colony cells, which results in collar microvilli flaring out. This result is consistent with a description of conraction the cell apex with changes in collar angle for *C. perplexa* cells [23]. Sheet inversion takes $\sim 10\,\mathrm{s}$. Notably, deviations in *C. perplexa* collar angle (between $10° − 90°$ from the apicobasal axis) were described in Ellis [12], and Leadbeater [24] described colonies now understood to be *C. perplexa* undergoing inversion. [1] Collar stiffness and the intrinsic curvature in collars facilitates a clear preference in sheet curvature. Collars in thecate cells have been described as flaccid [23], suggesting that an increase in collar stiffness is essential to the transition to colony-forming cells.

Brunet et al. [6] identified several factors that contribute or prohibit sheet inversion. It is believed that, in their natural environment, sheet inversion from flagella-in to flagella-out is triggered by darkness. In the inverted (flagella-out) state that occurs in darkness, individual cells demonstrated contraction of an apical actomyosin ring. The contraction results in collar microvilli flaring out: relative to the apicobasal axis measured at the base of the flagellum, the median collar microvillus angle moved out from $\sim 35°$ to $\sim 50°$. This increase in angle is largely the result of collar microvilli straightening out: in light, single colony-cells' collars curve to align with the apicobasal axis after emerging from the apical ends of cells.

---

[1]The latter attributes inversion to a reversal of flagellum rotation, though this explanation is unlikely given the more recent evidence for *C. flexa* [6].

> ak2351: add figure of individual cells

Cell sheet area decreases significantly since cell bodies are in contact in the inverted state [5]. These properties are summarised in figure 1.2b.

The transition to the flagella-out state results in a significant increase in swimming speed [6]. In contrast, flagella-in sheets are non-motile to the extent that they typically sink. The lack of mobility is compensated by an increase in cells phagocytosed by several times: flagella-in sheets are substantially more effective at driving flow towards the collars, where individual cells feed. Increased motility in the dark-induced state and accumulation in regions with light facilitates a primitive form of phototaxis.

> ak2351: why does swimming not directly translate to feeding as in lauga2011 paper?

Sheet inversion is rapid and reversible, allowing colonies the flexibility to convert when given suitable environmental cues.

> ak2351: discuss how larger sheets are harder to invert

Coordinated geometric changes in multicellular organisms are frequent, though they are typically achieved with several differentiated cell types or molecular signalling cascades [**?**].

1.4 Motivation and objective

As in the other basal model organisms used to probe the evolution of multicellularity, *C. flexa* provides a context to study the earliest driving factors towards multicellular shape change through cooperative individual action. In addition to sharing similar geometry with sponge choanocyte chambers and directly informing structural modeling there [2], *C. flexa* captures the close relationship between geometry and flow in biological settings.

> ak2351: add here

1.5 Thesis overview

C. flexa provides an opportunity to study geometric changes through a simple, uncoordinated mechanism in an evolutionarily basal context. In this thesis, I present several approaches for modeling *C. flexa* colony sheets from a mechanics perspective. I discuss relevant models from continuous mechanics and find that the simultaneous stretching and compression in several collar microvilli must be taken into account to appropriately model shape and dynamics. I review shape equations derived from variation of surface energies defined in terms of curvatures and derive an energy function for a continuous description of *C. flexa* sheets.

(a)

(b)

(c)
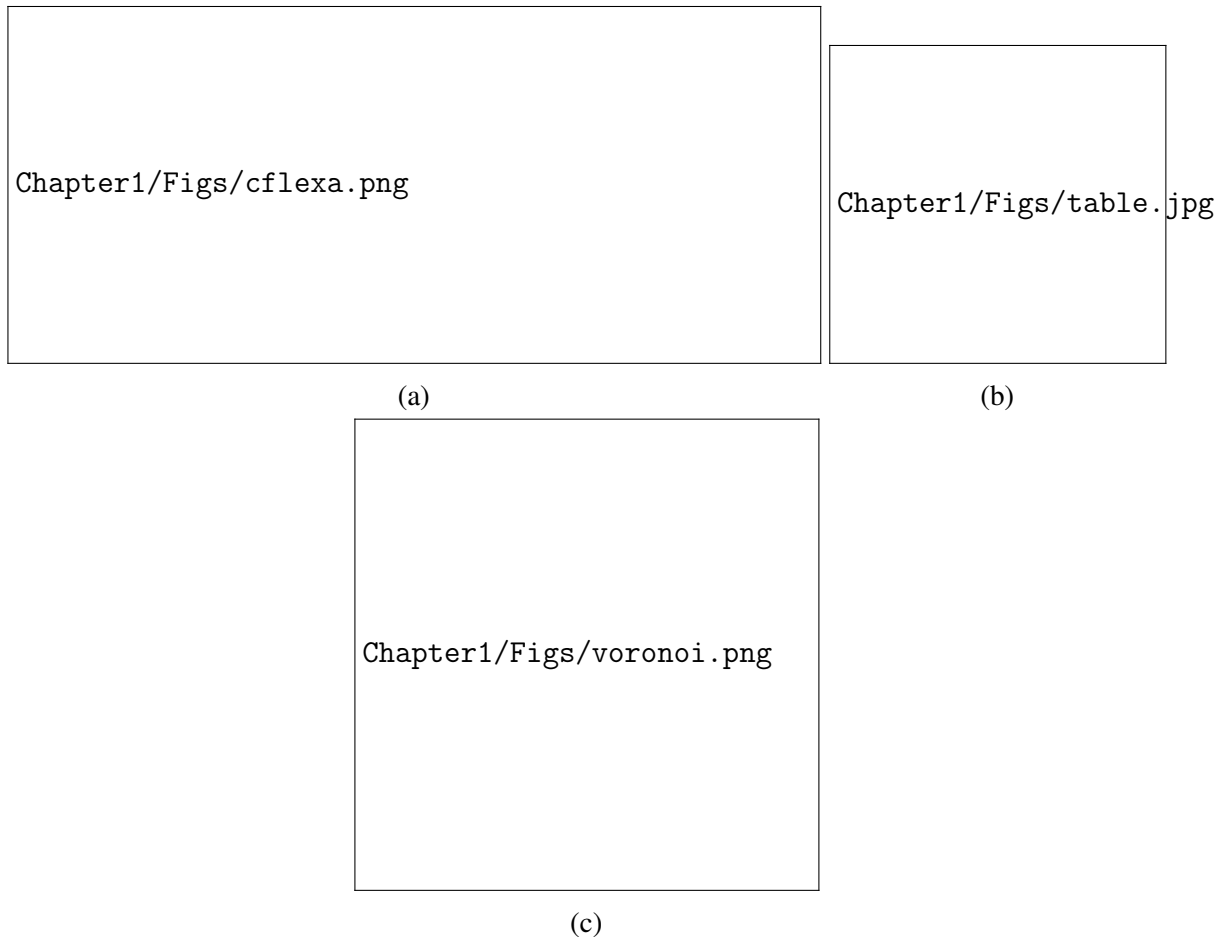
Fig. 1.2 Overview of *C. flexa* colonies of collared choanoflagellate cells. (1.2a) Images of the two conformations observed, flagella-in and flagella out. (1.2b) Summary of the two states of *C. flexa* colonies. The transition from flagella-in to flagella-out is induced naturally by darkness, and the reverse transition is induced by the reintroduction of light [6]. (1.2c) Transmission electron micrograph of collar interactions between neighboring cells. f: flagella, m: microvilli. A similar figure is presented in Leadbeater [24] for *C. perplexa*. figures 1.2a and 1.2c from Brunet et al. [6]. Reprinted with permission from AAAS.

Due to the complexity of the continuous model, I develop a more tractable discrete model based on lessons from the continuous description. Collar microvilli are simplified from filaments to elastic rods, which permits a simple energy function to be defined in terms quadratic potentials on cell-collar distances and angles defined by connecting cells and collars. The model consists of two parameters: equilibrium angles ϕ_0 (preferred angle from the collar base to the apicobasal axis) and ψ_0 (preferred collar-collar contact angle). I take the gradient of the energy with respect to cell and collar coordinate vectors as well as the apicobasal axis vectors of all cells to solve the forces acting on all free variables in the system. I numerically intergrate the forces on all spatial coordinates and torques on cell axes to study dynamics of cell sheets and study their mechanical equilibria.

My discrete model for *C. flexa* colonies successfully models inversion in small sheets consisting of few cells. In larger sheets, conformational changes are hindered by rings of cells which cannot undergo the requisite stretching or compression required for inversion or folding. For sheets with too many cells at the boundary, the inability to compress results in buckling at the edges. When sheets are already curved with flagella pointing in or out, the inability to sufficiently stretch at the boundary prevents sheets from inverting and causes the cells on the sheet interior to experience substantial stress. By framing my discrete model of *C. flexa* using graph theory, I identify that the topology of the cell-cell connection network determines a sheet's ability to bend without buckling or overstretching. This finding and my structural results compare well with the understanding of geometric effects of topological defects in crystal lattices.

The model I present makes it possible to identify regions where equilibrium angles ϕ_0 and ψ_0 give minimal energy structures in the flagella-in and -out conformations. For values that facilitate a flagella-out structure, the flagella-out structure is lower in energy than the flagella-in structure when sheet size prevents inversion as expected. I argue that the greater amount of time required for larger sheets to invert is the result of a larger energetic barrier or smaller net internal forces, rather than greater hydrodynamic damping through drag. This effect from topological constraints at the sheet boundary explains the rapid contraction and slow inversion observed in large sheets in Brunet et al. [6]. My model supports the hypothesis that *C. flexa* sheets are able to invert as a result of extreme stretching at sheet boundaries or topological changes through collar-collar linkages temporarily breaking.

Chapter 2

Continuous model

Sheets of *C. flexa*, despite being discretely made up of individual cells, appear to take on curvature when looked at as a whole. In an effort to develop an analytically tractable model for sheets consisting of many cells and avoid buildilng a detailed network topology, I approximate here sheets of *C. flexa* using continuous functions.

I begin by developing a one-dimensional filament model with inversion dynamics, which demonstrates that azimuthal stretching is key to understanding the flipping process observed in Brunet et al. [6]. I proceed to describe a method for approximating sheets of *C. flexa* with two-dimensional surfaces and relate the collar-opening angle ϕ and collar-collar contact angle ψ to surface curvature. I write an expression for the sheet energy and vary it to derive a shape equation.

2.1   One-dimensional model

ak2351: Discuss when a continuous model is appropriate

We are interested in the problem of *Choaneca flexa* inversion. To build intuition, consider a chain of cells connected by their collar filaments like beads on a string. Supposing there are sufficiently many cells that the length contributed to the chain of cells by a single cell is small relative to the total length, we approximate the filament with a continuous function $\vec{r}(s)$ parameterised by arclength s. If the filament has preferred curvature κ_0, then the bending energy functional ε is given by

$$\varepsilon[\vec{r}(s)] = \frac{1}{2}A \int (\kappa - \kappa_0)^2 ds,$$

where the curvature κ is deduced from $\vec{r}(s)$ and A is the bending modulus.

If the filament is short relative to the characteristic bending length scale, we express the problem in the Mange representation by writing $\vec{r}(s) = (x, h(x))$ for a height function $h(x)$. The resulting energy is written in terms of the prescribed (signed) curvature H_0,

$$\varepsilon[\vec{h}(x)] = \frac{1}{2}A \int_0^L (h_{xx} - H_0)^2 dx. \tag{2.1}$$

Since the cells in this beads-on-a-chain description consist of large spheres connected by thin filaments, we postulate that the filament experiences isotropic drag with coefficient ζ in a viscous medium. As a result, we describe the dynamics with a functional derivative of the energy with respect to the changing height,

$$\zeta \vec{r}_t = -\frac{\delta \varepsilon}{\delta \vec{r}}$$

$$\zeta h_t = -\frac{\delta \varepsilon}{\delta h}. \tag{2.2}$$

Taking the functional derivative of equation 2.1, we find the energy change

$$\delta \varepsilon = A(h_{xx} - H_0)\delta h_x\big|_0^L - Ah_{3x}\delta h\big|_0^L + A \int h_{4x}\delta h ds \tag{2.3}$$

in terms of the boundary conditions of h.

For free boundary conditions (force- and torque-free edges) $h_{xx}(0,L) = 0 = h_{3x}(0,L)$, the boundary terms in equation 2.3 vanish and we are left with the equation of motion

$$\zeta h_t = -Ah_{4x}. \tag{2.4}$$

Equation 2.4 is nondimensionalised by re-expressing x as x/L and t as $t/(\frac{\zeta L^4}{A})$ (the labels x, t, h, H_0 are left unchanged for readability) to derive $h_t = -h_{4x}$ with boundary conditions $h_{xx}(0,1) = 0 = h_{3x}(0,L)$. It is clear that the ground state of equation 2.1 is given by a quadratic height function with quadratic term $\frac{1}{2}H_0 x^2$. Let $h_*(x) = -\frac{1}{2}H_0(x - \frac{1}{2})^2 + \frac{1}{8}H_0$ be one such ground state, and suppose $h(x,0) = -h_*(x)$. Note that the filament in $h(x,0)$ is not in the ground state since the curvature is given by H_0.

The dynamics of the displacement $g(x,t) = h(x,t) - h_*(x)$ is given by $g_t = g_{4x}$. If $g(x,t) = e^{-\sigma t} f(x)$ for some $f(x)$ and eigenvalue σ, we obtain the ordinary boundary value problem

$$\frac{d^4 f}{dx^4} = \sigma f \qquad \begin{cases} f''(0,1) = 0 \\ f'''(0,1) = 0. \end{cases} \tag{2.5}$$

It is clear that the general solution of f is $A\sin kx + B\cos kx + D\sinh kx + E\cosh kx$ [19]. As in Wiggins et al. [35], the derivatives $f''(0) = f'''(0) = 0$ give $A = D, B = E$. Moreover, the eigenvalues $\sigma = k^4$ are given by the sequence of solutions k_n to

$$\cos k - \frac{1}{\cosh k} = 0. \tag{2.6}$$

Equation 2.6 is plotted in Figure 2.1a along with the positions of the solutions k_n as solved numerically. The solution $k_0 = 0$ is omitted because it contributes a constant term to $h(x,t)$ that does not evolve in time. The eigenfunctions $w_n(x)$ with eigenvalues k_n^4 are normalized on the interval $[0,1]$ numerically, and the ratio A/B is given by $(\sinh k - \sin(k))/(\cosh k - \cos k)$. The first five eigenfunctions are shown in Figure 2.1b.

Chapter2/Figs/eq_roots.png

Chapter2/Figs/efuncs.png
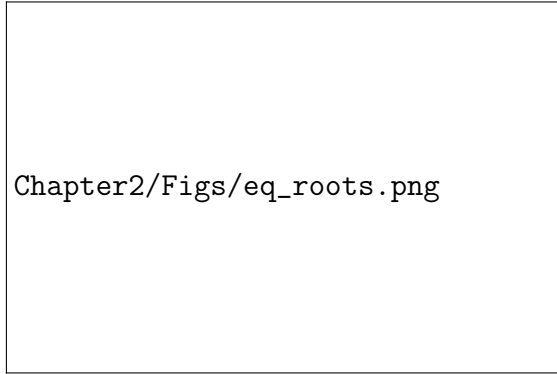
(a) Equation 2.6 and its solutions.
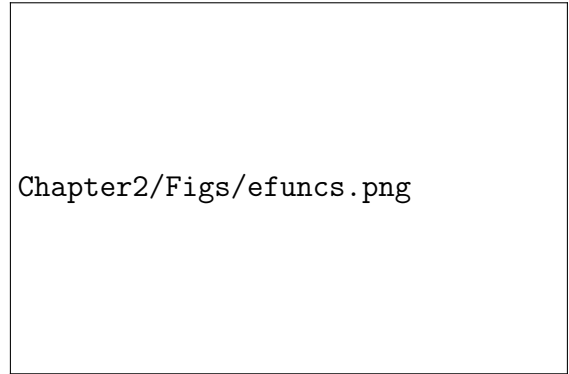
(b) The first five eigenfunctions f_n of boundary value problem 2.5.

Fig. 2.1 Solving the boundary value problem in equation 2.5

Letting $f(x) = \sum_{n=1}^{\infty} a_n f_n(x)$, we get that $a_n = \int_0^1 g(x,0) f_n(x) dx$, and the complete dynamics of the height function are given by

$$h(x,t) = h_*(x) + g(x) = h_*(x) + \sum_{n=1}^{\infty} a_n e^{k_n^4 t} f_n(x). \tag{2.7}$$

1   In practice, only the solutions k_n to equation 2.6 shown in Figure 2.1a are used, since the
2   approximation to $h(x, 0)$ is close and higher k_n result in precision errors when calculating
3    $\cosh kx$ and $\sinh kx$.

4   For the initial conditions given previously, the time evolution of $h(x, t)$ is shown in Figure
5   2.2. Immediately, we notice that the filament changes shape extremely quickly, and the
6   timescale $\zeta L^4 / A$ must be extremely large to produce inversion at the order of $10 \sec$ as
7   observed by Brunet et al. [6]. Using Stokes' law $\zeta = 6 \pi \mu R$ for dynamic viscosity μ (about
8    $1 \, \text{kg/m/sec}$ [33] and cell radius $R \approx 1 \times 10^{-6} \, \text{m}$ [6], a chain of 100 cells each contributing
9    $5 \times 10^{-6} \, \text{m}$ length would require energy constant about
10
ak2351: finish the above. compare to bending modulus of flagella or microtubule or somethin

11   Besides the issue of timescale, the dynamics in figure 2.2 also fail to capture the *rolling*
12   *over* phenomenon observed at the edges of large sheets [6], where a wave of changing
13   curvature propagates from the edge of the sheet towards the centre. While the edges show a
14   slight rim around $t \approx 9 \times 10^{-4}$, the effect is not as pronounced as in *C. flexa* inversion and
15   does not occur at the initation of the transition. A possible explanation for this effect in the
16   cell sheets is that the collars resist compression or stretching. The representation used here,
17   on the other hand, does not penalise filament compression.

18   As the arclength decreases substantially during the transition in figure 2.2 without affect-
19   ing its dynamics, it is clear that collar extension and compression are essential to describing
20   appropriate dynamics. Moreover, the timescales between this one-dimensional model and
21   those observed experimentally being as misaligned as they are indicates that some energetic
22   barrier to inversion is missing in the above description. We identify here the key deficiency of
23   the one-dimensional description of *C. flexa* sheets, which is that compression and extension,
24   especially in the azimuthal direction, are essential to understand the sheets' bistable nature.

25   ## 2.2   Surface approximation

26   The simplified dynamics that we get from the Mange representation lack energetic costs from
27   the compression and extension that come with deforming a two dimensional surface. The
28   logical step to include these energies is to model the flexa sheet a surface of revolution based
29   on a curve $\boldsymbol{r}(\rho, \theta) = (\rho \cos \theta, \rho \sin \theta, z(\rho))$ with cylindrical coordinates ρ, θ and height
30   function z. In doing so, we could take the elastohydrodynamic equation of motion written in
31   terms of curvature H and K and express it as purely as a function of z.

32   We will proceed by writing the equations of motion generally for a surface and reducing
33   it to a surface of revolution.
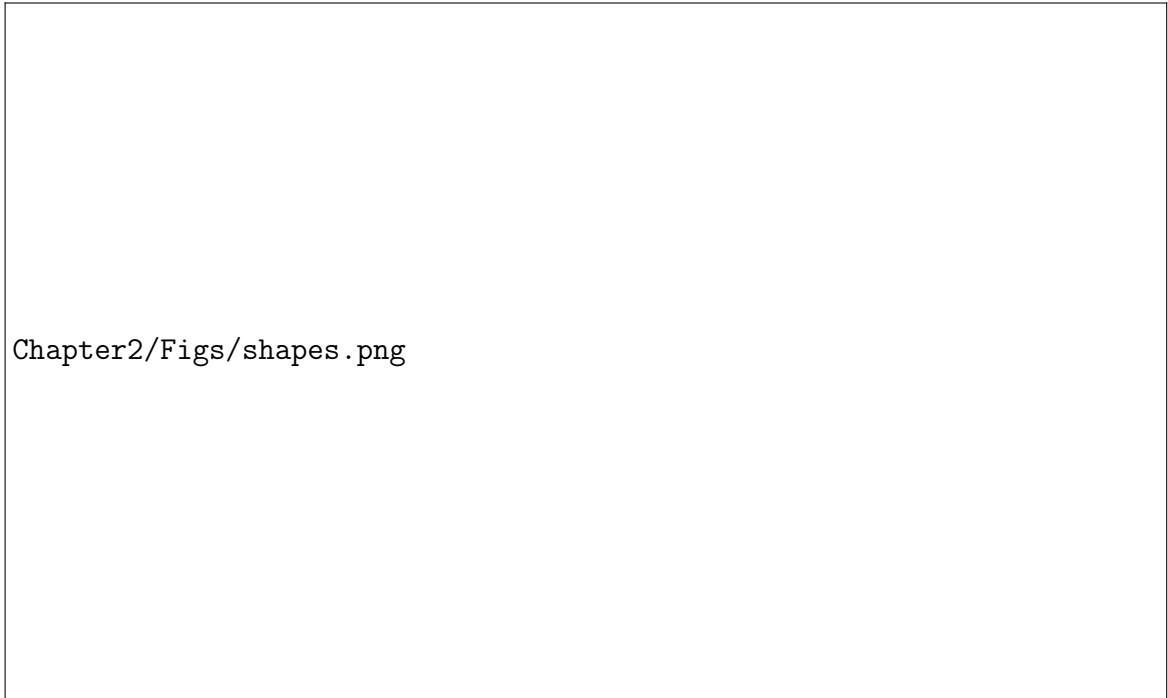
Fig. 2.2 Time evolution of a one-dimensional filament which switches prescribed curvature sign instantaneously. Time and length are given in dimensionless units defined by the length L, bending modulus A, and drag coefficient ζ. The time unlabeled time intervals continue sequentially in intervals of $\Delta t = 3 \times 10^{-4}$.

2.2.1   *H* and collar connection angle

Before getting into the continuous sheet problem, it is worth describing the two degrees of freedom that our collar connections afford. The collar makes an angle ϕ between the vector pointing directly out of the cell and the vector between the cell and its collar boundary with the next cell. Additionally, there is an angle between the collars of two adjacent cells ψ. The latter results in the sheet's curvature, so we want to relate it to mean curvature H or preferred curvature H_0.

> ak2351: Discuss why we need a collar angle ψ despite Brunet et al. [6] and other sources just talking about ϕ. This has to do with the straight-collar approximation that I use, where the collar shape and curvature + clamped boundary condition of the meeting collars is distilled into two angles

Chapter2/Figs/hpsi.jpg

Fig. 2.3 Geometry for relating collar boundary angle ψ to curvature H.

Consider two neighboring cells with collar boundaries a, b, and c, as shown in Figure 2.3. We might imagine defining a radius of curvature by the circle that passes through the three collar boundaries. If we set $\boldsymbol{x_a} = 2\ell \sin \phi_0(-1,0)$, $\boldsymbol{x_b} = (0,0)$, and $\boldsymbol{x_c} = 2\ell \sin \phi_0(\sin(\psi_0 - \phi_0), \cos(\psi_0 - \phi_0))$, we can solve for the circle coordinates

$$(x_\circ, y_\circ) = \ell \sin\phi_0 \left(-1, \frac{1 + \cos 2(\psi_0 - \phi_0)}{\sin 2(\psi_0 - \phi_0)} \right)$$

to get the inverse radius of curvature

$$H_0 = \frac{1}{\sqrt{x_\circ^2 + y_\circ^2}} = \frac{\sin(\psi_0 - \phi_0)}{\ell \sin\phi_0}. \tag{2.8}$$

This has a nice, simple interpretation in that if $\psi_0 > \phi_0$, $H_0 > 0$ (as drawn in Figure 2.3). On the other hand, $\psi_0 < \phi_0$ implies $H_0 < 0$, or the sheet is concave on the cell body side. Alternatively, we solve for ψ_0 as a function of H_0,

$$\psi_0 = \phi_0 + \arcsin\left(H_0 \ell \sin\phi_0\right). \tag{2.9}$$

As we find later in equation 2.14, the curvature of the sheet in any given direction is greater than or equal to $-1/\ell$ (cell bodies and collars cannot go through each other). This lower bound corresponds in 2.9 to $\psi_0 = 0$, which we expect when cells are pressing tightly against each other (Figure 2.5).

2.2.2   Problem statement

Powers [28] (Section IV.B) shows that for an energy density $\mathscr{E}$ written in terms of the first and second fundamental forms $g_{\alpha\beta}$ and $K_{\alpha\beta}$, we can write an expression for the stress tensor $\boldsymbol{F}^\alpha$

$$\boldsymbol{F}^\alpha = \left(T^{\alpha\beta} + \mathscr{E}^{\alpha\beta} K_\gamma^\beta \right) \boldsymbol{t}_\beta - (\nabla_\beta \mathscr{E}^{\alpha\beta}) \hat{\boldsymbol{n}}. \tag{2.10}$$

Here, $K_\gamma^\beta = K_{\gamma\delta} g^{\delta\beta}$, $\boldsymbol{t}_\beta = \partial_\beta \boldsymbol{r}$, and

$$T^{\alpha\beta} = g^{\alpha\beta} \mathscr{E} + 2 \frac{\partial \mathscr{E}}{\partial g_{\alpha\beta}} = \frac{2}{\sqrt{g}} \frac{\partial}{\partial g_{\alpha\beta}} \left(\sqrt{g} \mathscr{E} \right)$$

$$\mathscr{E}^{\alpha\beta} = \frac{\partial \mathscr{E}}{\partial K_{\alpha\beta}}$$

1 with $g = \det g_{\alpha\beta}$.

2   Since the force $\boldsymbol{f}$ acting on a surface point is given by the covariant divergence of the

3 stress $\nabla_\alpha \boldsymbol{F}^\alpha$, our problem is effectively solved once we decide on an appropriate energy

4 density. Brunet et al. [6] showed that the angle formed by the *C. flexa* collars changes when

5 individual cells are triggered for inversion. We might reasonably suggest preferred sheet

6 curvature is prescribed by changing the preferred angle of the collar ϕ_0 and imposing and

7 energetic cost based on the amount that the collar angle $\phi(\theta)$ differs around the collar in θ:

8 $\mathscr{E} \sim \int (\phi(\theta) - \phi_0)^2 d\theta$.

9 2.2.3   Connecting continuous surface with individual cell mechanics

10 For any point on a smooth surface, we could find an orthonormal basis of eigenvectors $\boldsymbol{e}_1, \boldsymbol{e}_2$

11 in the tangent space that diagonalises K^ν_μ. In terms of a vector $\boldsymbol{\Delta\xi}$ written in this basis, we

12 have that the change in height with respect to the tangent plane and its normal Δh is given by

13 $K_{\mu\nu}\Delta\xi^\mu\Delta\xi^\nu$.

14   Let's consider a cell with collar angle $\phi(\theta)$, where θ measures the location on the collar.

15 If the cell has an optimal collar angle ϕ_0 and corresponding optimal curvature $K_{0\mu\nu}$, then the

16 height of the collar will be $K_{0\mu\nu}\Delta\xi_0^\mu\Delta\xi_0^\nu$. The distance from the centerline of the cell (the

17 norm of $\boldsymbol{\Delta\xi_0}$) is determined by ϕ_0. The geometry is shown in Figure 2.4.

18   If the cell has collar angle ϕ in direction θ, we know the collar distance as $\boldsymbol{\Delta\xi} =$

19 $\ell(\cos\phi, \sin\phi)$. For a fixed collar length ℓ, we know the difference in height between the

20 ground state and deformed state is $\ell(\cos\phi - \cos\phi_0)$. We can then relate the collar angle and

21 sheet curvature by equating

$$K_{\mu\nu}\Delta\xi^\mu\Delta\xi^\nu - K_{0\mu\nu}\Delta\xi_0^\mu\Delta\xi_0^\nu = \ell(\cos\phi - \cos\phi_0). \tag{2.11}$$

24   The radius out from the center for the ground state is $\ell\sin\phi_0$ while for the deformed state

25 it is $\ell\sin\phi$, so for $K_{011} = K_{022} = H_0$, we get

$$K_{\mu\nu}\ell^2\sin^2\phi(\cos\theta, \sin\theta)^{\mu,\nu} - H_0\ell^2\sin^2\phi_0 = \ell(\cos\phi - \cos\phi_0)$$

$$H_\theta\ell^2\sin^2\phi - H_0\ell^2\sin^2\phi_0 = \ell(\cos\phi - \cos\phi_0)$$

29 where $H_\theta = K_{11}\cos^2\theta + K_{22}\sin^2\theta + 2K_{12}\sin\theta\cos\theta$ is the curvature of a line on the surface

30 in direction θ. We can cancel a factor of ℓ, redefine units of length in terms of ℓ (such that
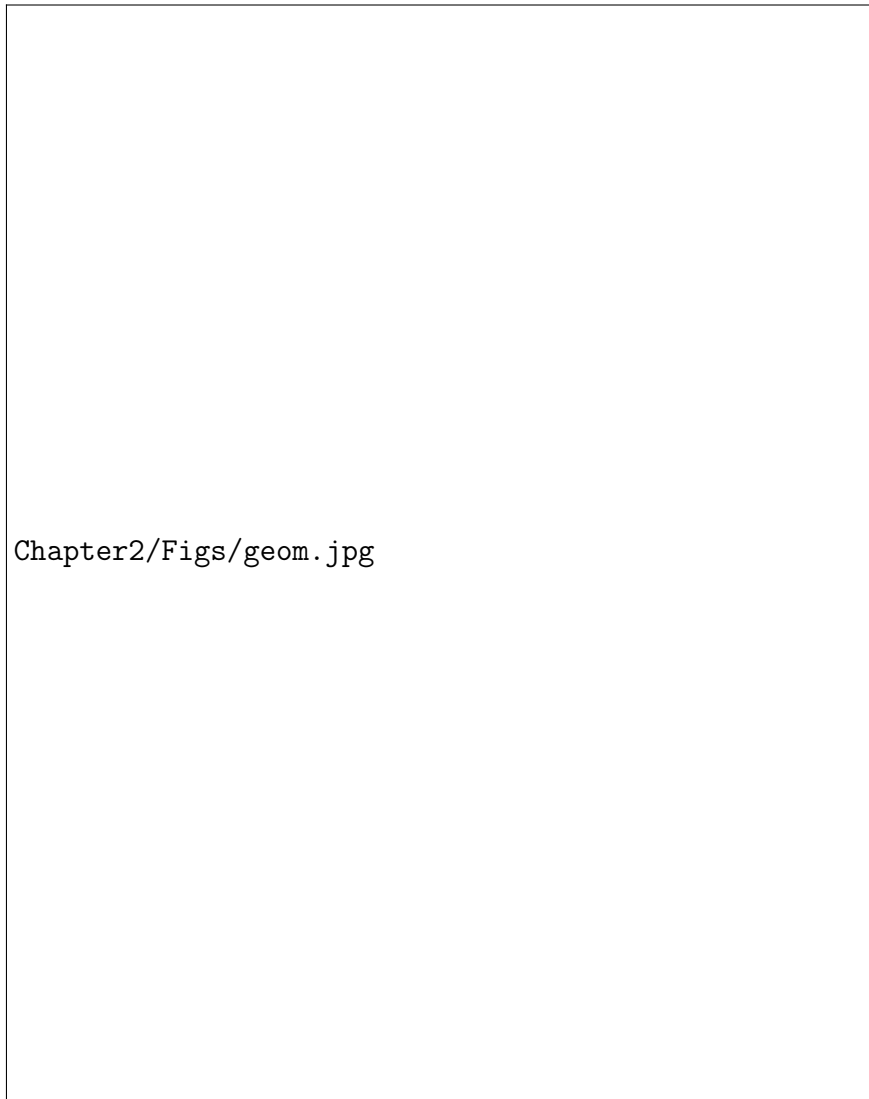
Fig. 2.4 Geometry of a single cell and collar with a continuous surface approximating the interactions between collars.

H_θ is the ratio of ℓ with the radius of curvature in direction θ), and express $\sin^2 \phi$ in terms of $\cos \phi$ to get

$$0 = H_\theta \cos^2 \phi + \cos \phi + (H_0 \sin^2 \phi_0 - \cos \phi_0 - H_\theta)$$

$$\cos \phi = \frac{-1 \pm \sqrt{1 + 4H_\theta(H_\theta + \cos \phi_0 - H_0 \sin^2 \phi_0)}}{2H_\theta}.$$

If we take the collars to always have angle $0 \leq \phi \leq \pi/2$, we can constrain $0 \leq \cos \phi \leq 1$ to find the two inequalities

$$H_\theta \geq H_0 \sin^2 \phi_0 - \cos \phi_0 \tag{2.12}$$

$$1 \geq \cos \phi_0 - H_0 \sin^2 \phi_0. \tag{2.13}$$

The second inequality can be simplified to $H_0 \geq -(1 + \cos \phi_0)^{-1}$. Combining the two inequalities yields

$$H_\theta \geq -1. \tag{2.14}$$

Re-expressed with units, this means that $H_\theta \geq -1/\ell$, or that the radius of curvature can never be smaller than ℓ on the cells' side. In other words, the cells can't push through each other! (Figure 2.5)

Fig. 2.5 Maximum cell-side curvature is given by inequalities 2.12, 2.13 to have radius ℓ. This corresponds to every (point) cell bumping into each other.

2.2.4   Writing the energy

We want to write equation 2.11 in terms of $\phi - \phi_0$ to write down the energy. We can use a trigonometric identity to write

$$H_\theta \sin^2 \phi - H_0 \sin^2 \phi_0 = -2 \sin \frac{\phi - \phi_0}{2} \sin \frac{\phi + \phi_0}{2}. \tag{2.15}$$

If $phi - phi_0$ is small in magnitude, then

$$\sin \frac{\phi - \phi_0}{2} \approx \frac{\phi - \phi_0}{2}$$

$$\sin \frac{\phi + \phi_0}{2} = \sin \left(\phi_0 + \frac{\phi + \phi_0}{2} \right) \approx \sin \phi_0 + \frac{\phi - \phi_0}{2} \cos \phi_0$$

$$\sin^2 \phi = \sin^2 (\phi_0 + (\phi - \phi_0)) \approx \sin^2 \phi_0 + (\phi - \phi_0) \sin 2\phi_0.$$

Using these approximations we rewrite equation 2.15 to first order in $\phi - \phi_0$ as

$$(H_\theta - H_0) \sin^2 \phi_0 + H_\theta (\phi - \phi_0) \sin 2\phi_0 = -(\phi - \phi_0) \sin \phi_0$$

$$(H_\theta - H_0) \sin^2 \phi_0 = -(\phi - \phi_0)(H_\theta \sin 2\phi_0 + \sin \phi_0)$$

$$\frac{(H_\theta - H_0)^2 \sin^4 \phi_0}{(H_\theta + \sin \phi_0 / \sin 2\phi_0)^2 \sin^2 2\phi_0} = (\phi - \phi_0)^2.$$

We want to integrate this function in θ, so let $K_{11} = a$, $K_{22} = b$, $K_{12} = c$, $-H_0 = d$ and $\sin \phi_0 / \sin 2\phi_0 = e$ for simplicity when we write

$$\int_{-\pi}^{\pi} (\phi - \phi_0)^2 d\theta = \int_{-\pi}^{\pi} \frac{\left(a\cos^2\theta + b\sin^2\theta + 2c\sin\theta\cos\theta + d\right)^2}{\left(a\cos^2\theta + b\sin^2\theta + 2c\sin\theta\cos\theta + e\right)^2} d\theta$$

$$= \Big\{ -\sin 2\theta \left[a^2(-4bc\theta - 4ce\theta + d^2 - 2de + e^2) + a(4b^2c\theta - 2b(d-e)^2 + 4c\theta(c^2 - e^2)) \right.$$

$$\left. + b^2(4ce\theta + d^2 - 2de + e^2) + 4bc\theta(e^2 - c^2) + 4c^2(d-e)^2 \right]$$

$$+ 2(a+b+2e)\left[c^2\theta(b-a) + \theta(a-b)(a+e)(b+e) - c(d-e)^2 \right]$$

$$+ 2\theta(a-b)^2\cos(2\theta)(a(b+e) + e(b+e) - c^2) \Big\}$$

$$\big/ 2\left[(a-b)(a(b+e) + e(b+e) - c^2)((a-b)\cos(2\theta) + a + b + 2c\sin(2\theta) + 2e) \right]$$

$$+ \frac{(e-d)(a(4b+d+3e) + bd + 3be - 4c^2 + 2de + 2e^2)\tan^{-1}\left(\frac{-(b+e)\tan\theta - c}{\sqrt{a(b+e) + e(b+e) - c^2}} \right)}{2(a(b+e) + e(b+e) - c^2)^{3/2}}$$

evaluated at $\theta = -\pi, \pi$. Evaluating this expression is surprisingly straightforward, and gives
the result

$$\int_{-\pi}^{\pi} (\phi - \phi_0)^2 d\theta = \text{const.} + \text{const.} \frac{4K + 2(d+3e)H + 2de + e^2}{(K + 2H + e^2)^{3/2}}.$$

Varying this expression will be more difficult than the typical membrane energy defined
only in terms of curvature $(H - H_0)^2 + K$ since the Gaussian curvature term is not alone.
This means that we cannot use the Gauss Bonnet theorem $\int_S K dA = 2\pi n + \oint_{\partial S} K ds$ to simply
write it as a boundary term. Nevertheless, provided that we can vary K on the surface, the
shape equation that results shouldn't be very difficult to derive.

2.2.5   Varying the energy

Following subsection 2.2.2, we just need to express our energy in terms of $K_{\mu\nu}$ and $g_{\mu\nu}$
to derive a force from it. We of course have that $H = (1/2)(K_{\mu\nu}g^{\mu\nu})$, which is easily
differentiated with respect to $K_{\mu\nu}$ and $g_{\mu\nu}$. We can differentiate K by re-expressing it with
the identity $K^{\alpha\beta}K_{\alpha\beta} = 4H^2 - 2K$.[1] Then we have $K = (g^{\alpha\beta}K_{\alpha\beta})^2 - K_{\mu\nu}K_{\alpha\beta}g^{\mu\alpha}g^{\nu\beta}$.

---

[1]This comes from $4H^2 - 2K = (K_1^1 + K_2^2)^2 - 2(K_1^1K_2^2 - 2K_2^1) = (K_1^1)^2 + 2K_2^1K_2^1 + (K_2^2)^2 = K_\beta^\alpha K_\alpha^\beta = K^{\alpha\beta}K_{\alpha\beta}$.

2.3   Energy variation

Chapter 3

Discrete model

Models of organisms and population dynamics must be designed by either describing poten-
tially many discrete units[1] with continuous functions or dealing with the analytical complexity
of discretisation. Even with the continuous description of *C. flexa* described previously, nu-
merical solutions to the shape equations would require discretisation of a surface. Here, I
pursue a simplified, discrete description of *C. flexa* sheets. As in chapter 2, I proceed by for-
mulating an energy function based on the coordinate vectors of cells and vary it with respect
to the coordinates. This procedure results in expressions for the forces on the coordinates,
which can be forward integrated in time to study the dynamics and steady state geometries of
C. flexa sheets.

In addition to avoiding the complexity of describing surface curvatures H, K in a discrete
program, I find the force equations are relatively quite tractable. Expressing the gradient
of the energy as summations over collars belonging to each cell or cell-cell interactions
makes it possible to neatly arrange the force calculations as tensor index contractions or,
even more simply, matrix multiplications. Of course, describing choanoflagellate sheets as
discrete systems also remains faithful to real sheets, and this approach remains applicable
over colonies of all cell counts.

3.1 Discrete sheet description

The most natural framework to describe a interactions between a set of discrete points is
graph theory. Since colonies of *C. flexa* form sheets with two distinct sides and there is
no evidence to suggest that *Choanoeca* acts otherwise [6, 24], we are welcome to treat the

---

[1]in this case, cells

network of interactions between cells as a plane graph G. With cells $C = \{\alpha\}_{\alpha \in C}$ making up vertices and cell-cell interactions via collars $E = \{(\alpha, \beta)\}_{(\alpha, \beta) \in E}$ making up edges in a graph G, we describe which cells impart forces on each other.

However, we understand from the studies into *Choanoeca* that cells interact through their collars [12, 24, 6]. Guided by imaging in the sheet-tangential plane (figure 1.2c), we see that another natural planar graph G^* is that with edges along interfaces between cells' collars. [2] In this description, vertices mark the points at which the interface between a pair of cells $(\alpha, \beta) \in E$ ends. For a cell $\alpha \in C$ whose collar microvilli are all in contact with those of other cells, the vertices in G^* corresponding to cell α are points where α interacts with two or more cells simultaneously.
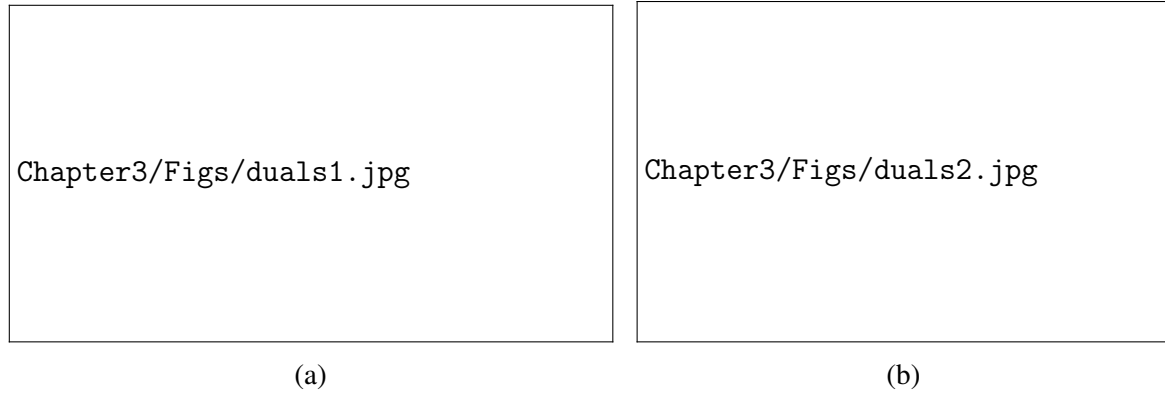
Fig. 3.1 Two views of the physical dual graphs used in describing *C. flexa*.

As each edge in G^* transects an edge (α, β) between cells α, β in G, we identify G^* as the dual graph of G (figure 3.1a). [3] Consequently, we have that either G or G^* is sufficient to specify the topology of the other provided the coordinates of vertices (figure 3.1b).

3.1.1 Defining a sheet

A reasonable simplification of the cell sheet will use either the cell-cell interaction graph G or the collar boundary edge graph G^*. Since physical interactions occur at the collar interfaces, I consider first the physical details of a model defined on G^*.

---

[2] Until noted otherwise, I treat the several collars interacting between two cells as a continuous line of interaction with infinitesimal collars spanning the cells' interface. The implications of this choice are discussed later.

[3] As G is finite, all vertices in G^* as described above which indicate two cells' interactions ending at the edge of a colony sheet would be merged into a single vertex v_* in the dual graph of G. Consequently G^* is not exactly the dual graph of G. We address this later when defining sheet edges numerically by replacing each edge (v, v^*) in G^* with the edge (v, v') for new vertices v' and removing v_* from G^* and deleting all edges incident on v_*.

The physical interactions happen at the collar boundaries, so it makes sense to define energy based on the graph G^* that describes them. If two cells have a collar boundary described by $\boldsymbol{r}_\rho t + (1-t)\boldsymbol{r}_\sigma$ with $0 \leq t \leq 1$ and the energy is defined by continuously many springs from the boundary to a projected cell point $\boldsymbol{r}_\alpha^*$, then the energy $E_{\rho\sigma}$ of that boundary is

$$E_{\rho\sigma} = \int_0^1 \left[(\boldsymbol{r}_\rho t + (1-t)\boldsymbol{r}_\sigma) - \boldsymbol{r}_\alpha^* \right]^2 dt = \frac{1}{3}(\boldsymbol{r}_\rho + \boldsymbol{r}_\sigma)^2 - \frac{1}{3}\boldsymbol{r}_\rho \cdot \boldsymbol{r}_\sigma - \boldsymbol{r}_\alpha^* \cdot (\boldsymbol{r}_\sigma + \boldsymbol{r}_\sigma) + \boldsymbol{r}_\alpha^{*2}.$$

$$(3.1)$$

The energy corresponding to a cell consists of the line energies of all the collar interfaces. We find the position $\boldsymbol{r}_\alpha^*$ by setting the gradient of equation 3.1 with respect to $\boldsymbol{r}_\alpha^*$ to zero for all lines $\rho\sigma$. If ρ indexes the vertices that cell α has (which I denote $\rho \in \alpha$ for the remainder of this chapter), then

$$0 = \frac{dE}{d\boldsymbol{r}_\alpha^*} = -\sum_{\rho \in \alpha} \boldsymbol{r}_\sigma + 2n\boldsymbol{r}_\alpha^*$$

$$\boldsymbol{r}_\alpha^* = \frac{1}{n}\sum_{\rho \in \alpha} \boldsymbol{r}_\rho.$$

The force on vertex σ is then given by the gradient of the whole sheet energy E_{sheet}, which is the sum of the energies E_α corresponding to each cell α.

$$\frac{d\mathcal{E}_{\text{sheet}}}{d\boldsymbol{r}_a} = \frac{d}{d\boldsymbol{r}_a}\sum_{\Delta} \mathcal{E}_\Delta = \sum_{\Delta : a \in \Delta} \frac{d\mathcal{E}_\Delta}{d\boldsymbol{r}_a} = \sum_{\Delta : a \in \Delta} \frac{d}{d\boldsymbol{r}_a}\sum_{b \in \Delta} (\boldsymbol{r}_b - \boldsymbol{r}_\Delta)^2.$$

Since $\boldsymbol{r}_\Delta$ depends on $\boldsymbol{r}_a$ itself, we write

$$\boldsymbol{f}_{\text{on } a} = -\sum_{\Delta : a \in \Delta} \frac{d}{d\boldsymbol{r}_a}\sum_{b \in \Delta} \left(\boldsymbol{r}_b - \frac{1}{n}\sum_{c \in \Delta} \boldsymbol{r}_c \right)^2$$

$$= \sum_{\Delta : a \in \Delta}\sum_{b \in \Delta} \left(2\boldsymbol{r}_a \delta_{ab} - \frac{2}{n}\sum_{c \in \Delta} (\boldsymbol{r}_c \delta_{ab} + \boldsymbol{r}_b \delta_{ac}) + \frac{1}{n^2}\sum_{c \in \Delta}\sum_{d \in \Delta} (\delta_{ac}\boldsymbol{r}_d + \delta_{ad}\boldsymbol{r}_c) \right)$$

$$= -2(\boldsymbol{r}_a - \boldsymbol{r}_\Delta)$$

This process was overkill, since we could have reasonably assumed that r_Δ would be at the vertices' center of mass and that we'd effectively get springs from r_Δ to each vertex. This is thanks to linearity of the collar springs. However, assuming that the collars have a positive equilibrium length r_0 makes it necessary to go through the above procedure.

If instead the line energy is

$$\mathscr{E}_{ab} = \int_0^1 \left(|r_a t + (1-t) r_b - r_\Delta| - r_0 \right)^2 dt,$$

then the cell position r_Δ is the solution to

$$0 = -2 \sum_{b \in \Delta} r_b + 6 r_\Delta - 2 r_0 \frac{d}{dr_\Delta} \sum_{(b,c) \text{ edge in } \Delta} \int_0^1 |r_b t - (1-t) r_c - r_\Delta| \, dt$$

$$0 = -2 \sum_{b \in \Delta} r_b + 6 r_\Delta - 2 r_0 \sum_{(b,c)} \int_0^1 \frac{r_\Delta - r_c - t(r_b - r_c)}{|r_b t - (1-t) r_c - r_\Delta|} \, dt.$$

We can actually evaluate the integral above, but I found that it gives a transcendental equation for r_Δ and decided it wasn't pursuing further on paper. Nonzero equilibrium length springs is better pursued numerically. Alternatively, we simply define springs from r_Δ to each dual graph vertex rather than making the collars consist of continuous springs.

Bending

One way to define a bending energy is to give each cell a vector that corresponds to the midline pointing out from the center of the cell, which I have implicitly drawn in the figures of individuals flexas. From there, we could reasonably define a bending energy from the interactions between two interacting flexas by the angle between their corresponding "normal" vectors weighted by the length of their interface.

Defining an individual vector is made complicated by the fact that the vertices along the cycles corresponding to each flexa are not necessarily coplanar, provided that a given cell is interacting with more than three other cells. One option, although I have not developed it, is to find the plane whose summed mean squared distances to each vertex for a cell is minimised. It would possibly be more accurate to again treat the edges as lines and minimise the integrated distance from the normal plane to the edges. Either way, the energy dictated by the angle between adjacent normal vectors will need to be summed over all pairs of

neighboring cells, namely all edges in the graph where edges correspond to cell neighbors
(not collar interfaces).

3.1.2   Surface formed by cell bodies

The graph of cell bodies and neighbor edges makes it easy to work with springs, but it is less
clear how to define a bending energy. The math for springs is identical to previously, so let's
just think about how to define bending energy.

> ak2351: needs more work

3.1.3   Numerically specifying initial conditions

For sheets whose graph of cell-cell connections G can be drawn on a plane with edges as
straight lines, it is simplest to define the initial spatial graph G as lying in the *xy*-plane with
cell coordinates $\{r_\alpha\}_{\alpha \in C}$ and to use Voronoi tessellation to generate collar vertices in G^*.
Voronoi tessellation allows for generalisation beyond regular lattices, though it does not
facilitate graph topologies that cannot be drawn in a plane as described above.

   To build more complex graphs G that are nevertheless planar, we can either use subsets
of common polyhedra (e.g. subdivided icosahedron) or triangulate points that lie along a
surface. In the latter case, I found sufficient flexibility in randomly sampling a specified
number of points uniformly distributed on a sphere below some latitude, then calculating
the generalised Voronoi tessellation with respect to the metric on the sphere as described in
Caroli et al. [7].

> ak2351: add a figure showing the various initial conditions

   We build introduce vertices from G^* where two cells' collar microvilli diverge to build a
larger graph $\mathfrak{G}$ consisting of cell-cell interaction edges (α, β) from G and cell-collar edges
(α, ρ) between cells α and collar edges $\rho \in \alpha$. Here, $\rho \in \alpha$ denotes a collar vertex ρ from
G^* connecting to cell α via the cell's microvilli. With cell positions r_α already specified and
cell-cell interactions given from G, collar vertex positions r_ρ of collar vertices connecting
to three cells are initially set as the centroid of the three cells plus the normal vector of the
triangle they form. The orientation of the normal vector is set to be consistent across the
sheet, such that all collar vertices are positioned on the same side of the sheet, as all cells in
C. flexa colonies face the same direction.[4]

---

[4]Since I use Voronoi triangulation to collar vertices, at most three cells interact at any collar vertex. This is
a consequence of the dual of Voronoi tesselation being Delaunay triangulation.

1   As Voronoi diagrams for finitely many cells include ridges that extend out to infinity,
2 and the spherical Voronoi algorithm on points below a given latitude on the sphere produces
3 ridge vertices above that latitude, collar vertices at the boundary of the sheet must be added
4 manually. I call these collar vertices at the edges as *boundary collars*. Before choosing to
5 add these vertices, we must first consider how collar interactions at the boundary affect sheet
6 energy.
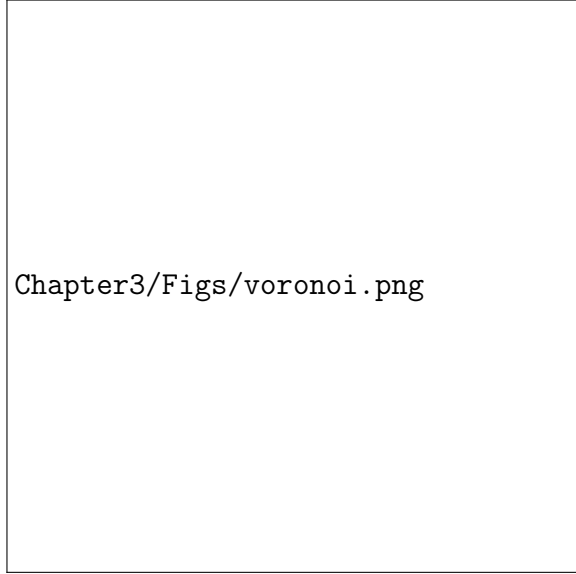
Fig. 3.2 Voronoi tesselation of initial cell placement. Cell bodies shown in blue points, collar boundaries shown in black lines with collar boundary end points shown in orange. Notably, the regions corresponding to boundary cells extend out to infinity. We need to add all boundary collar vertices along the infinite dashed lines.

7 **Boundary collar vertices**

8 We ask whether boundary collar vertices contribute to the energy. For boundary cells α, β,
9 suppose the line of physical interactions between the two cells' microvilli spans from point
10 r_ρ and ends at point r_σ. We with to know how the angle between the planes given by points
11 ρ, α, σ and ρ, β, σ changes with the position of boundary collar vertex σ.
12   Suppose for the time being that the collar length is fixed at ℓ, so the possible values
13 for r_σ are constrained. We simplify the problem by reparameterising our coordinates such
14 that $r_\alpha = (-1, 0, 0)$, $r_\rho = (0, r, 0)$, and $r_\beta = (1, 0, 0)$, where $r = \sqrt{\ell^2 - 1}$. Here, ℓ is a
15 dimensionless ratio of the collar length to half the cell-cell distance. We readily see that
16 $r_\sigma = (x, y, z)$ is constrained to take values in the circle defined by $r^2 = y^2 + z^2, x = 0$.

Parameterising the positions of $\boldsymbol{r}_\sigma(\theta) = (0, r\cos\theta, r\sin\theta)$ by angle θ with the second
axis, we find the normals for planes ρ, α, σ and ρ, β, σ as

$$
\hat{\boldsymbol{n}}_{\rho\alpha\sigma} = (\boldsymbol{r}_\sigma - \boldsymbol{r}_\alpha) \times (\boldsymbol{r}_\rho - \boldsymbol{r}_\alpha)
$$

$$
= \frac{(-r^2\sin\theta, r\sin\theta, r - r\cos\theta)}{r^4\sin^2\theta + 2r^2(1 - \cos\theta)}
$$

$$
\hat{\boldsymbol{n}}_{\rho\beta\sigma} = (\boldsymbol{r}_\rho - \boldsymbol{r}_\beta) \times (\boldsymbol{r}_\sigma - \boldsymbol{r}_\beta)
$$

$$
= \frac{(r^2\sin\theta, r\sin\theta, r\cos\theta - r)}{r^4\sin^2\theta + 2r^2(1 - \cos\theta)}.
$$

After simplifying, the angle between these two normal vectors is

$$
\hat{\boldsymbol{n}}_{\rho\alpha\sigma} \cdot \hat{\boldsymbol{n}}_{\rho\beta\sigma} = 1 - \frac{2}{1 + \frac{1}{2r^2}\left(1 + \tan^2\frac{\theta}{2}\right)}. \tag{3.2}
$$

It is clear that the position of the boundary collar interaction at $\boldsymbol{r}_\sigma$ changes the angle
between these two planes, given by the arccosine of equation (3.2). In the simplified sheet
structure defined in the combined cell-collar graph $\mathfrak{G}$, this results in a change in energy based
on the position of $\boldsymbol{r}_\sigma$. Consequently, as the notation indicates, boundary collar vertices are
introduced to $\mathfrak{G}$ connecting between each pair of boundary cells.

Adding boundary collar vertices

Defining initial positions for boundary collar vertices becomes challenging when sheets are
not planar, though a reasonable placement is sufficient since the positions will be changed
later. For sheets in the *xy*-plane generated by 2-dimensional Voronoi tesselation (figure 3.2),
ridges extending out to infinity are removed and replaced with collar vertices at finite distance.
The position of a boundary collar vertex σ between cells α, β is calculated as follows. First,
a unit vector $\hat{\boldsymbol{n}}$ perpendicular to the ridge between cell positions $\boldsymbol{r}_\alpha, \boldsymbol{r}_\beta$ is determined. For
sheets in the *xy*-plane, $\hat{\boldsymbol{n}} = \hat{z}$. Otherwise, $\hat{\boldsymbol{n}}$ is simply aligned with the average of the normal
vectors $\hat{\boldsymbol{n}}_\alpha, \hat{\boldsymbol{n}}_\beta$. Then, the boundary collar vertex position $\boldsymbol{r}_\sigma$ is positioned at the reflection of
$\boldsymbol{r}_\rho$ over the plane given by points $\boldsymbol{r}_\alpha, \boldsymbol{r}_\beta, \boldsymbol{r}_\alpha + \hat{\boldsymbol{n}}$, where ρ is the existing collar vertex shared
by α and β. Notably, this process results in a boundary collar position $\boldsymbol{r}_\sigma$ farther from the
center of the sheet than $\boldsymbol{r}_\rho$ and equidistant to $\boldsymbol{r}_\alpha, \boldsymbol{r}_\beta$ as $\boldsymbol{r}_\rho$.

1   This process produced reasonable boundary collar vertex positions to initialise sheet

2   dynamics simulations (figure 3.3). For initial collar positions not too far from cells, collars

3   did not overlap or cross over each other. Some initial graphs 𝔊 are shown projected onto the

4   *xy*-plane, though the collars are offset in *z* (**??**) or the entire sheet is not necessarily lying in

5   the *xy*-plane (**??**).

6   ak2351: add to figure 3.3

Chapter3/Figs/layout_init.png

Fig. 3.3 Initial layout for the flexa sheet. Cell bodies are shown in large purple points and collar boundary vertices are shown in small yellow points. Black edges connect cells to collar boundary vertices, and orange edges show cell-cell neighbor relations (though these orange edges are not physically present). The physical interactions are mediated through the black edges.

3.2   Sheet energy

In developing the simplified, discrete model for *C. flexa* as a spatial graph, I aim to distill the complex physics of collar-collar interactions into a minimum number of sufficient energy terms to capture the sheet bending that we observe experimentally. In what follows, I treat edges (α, ρ) between a cell α and collar vertex ρ as straight line collar microvilli and cell pairs, flanking collar pairs $(\alpha, \beta : \rho, \sigma)$ as lines of interactions between the planes given by points ρ, α, σ and ρ, β, σ.

Consequently, as detailed in the continuous model description of chapter 2, I build an energy function $\mathscr{E}$ that penalises deviations for angles ϕ and ψ, which describe angles between (ϕ) collar microvilli and cell normal vectors $\hat{\boldsymbol{n}}_\alpha$ and (ψ) plane normals $\hat{\boldsymbol{n}}_{\rho\alpha\sigma}, \hat{\boldsymbol{n}}_{\rho\beta\sigma}$.

3.2.1   Cell-collar angle energy

Cell normal definition

For a physical *C. flexa* cell α with fixed position $\boldsymbol{r}_\alpha$ and fixed collar positions $\{\boldsymbol{r}_\rho\}_{\rho \in \alpha}$, we realise that the cell still has freedom in its rotation which we expect will contribute substantially to its energy. In other words, there should be an optimal rotation for the cell to minimise its mechanical energy. Since we treat *C. flexa* cells as rotationally symmetric above the apicobasal axis, it suffices in our description to assign to each cell α in the graph $\mathfrak{G}$ a unit vector $\hat{\boldsymbol{n}}_\alpha$

For simplicity, each vector $\hat{\boldsymbol{n}}_\alpha$ is initially defined as the unit vector in the direction of $\sum_{\rho \in \alpha} \vec{\alpha\rho}$, where $\vec{\alpha\rho} = \boldsymbol{r}_\rho - \boldsymbol{r}_\alpha$.

Energy $\mathscr{E}_\phi$

Defining an energy term on the angle ϕ between a cell α's collars and the apicobasal axis $\hat{\boldsymbol{n}}_\alpha$ is established on descriptions of *Choanoeca* in the literature. Brunet et al. [6] describes the change in this angle as the result of exposure to light in *C. flexa*. Similarly, Ellis [12] characterises the variation in ϕ observed in individual cells of *C. perplexa*.

Consequently, we consider an energy term $\mathscr{E}_\phi(\{\boldsymbol{r}_\alpha, \hat{\boldsymbol{n}}_\alpha\}, \{\boldsymbol{r}_\rho\})$ which penalises devation from a common equilibrium basal collar angle ϕ_0:

$$\mathscr{E}_\phi(\{\boldsymbol{r}_\alpha, \hat{\boldsymbol{n}}_\alpha\}, \{\boldsymbol{r}_\rho\}) = \sum_{(\alpha,\rho)} \left(\phi_{(\alpha,\rho)} - \phi_0\right)^2. \tag{3.3}$$

1   The sum indicates summation over all cell-collar pairs (α, ρ) in the sheet $\mathfrak{G}$. The angle

2   $\phi_{(\alpha,\rho)}$ is calculated entirely based on the cell normal vector $\hat{\boldsymbol{n}}_\alpha$ and unit vector $\hat{\alpha\rho}$ pointing

3   in the direction of $\hat{\boldsymbol{r}}_\rho - \hat{\boldsymbol{r}}_\alpha$:

4   > ak2351: make this equation numbered and number other substantial equations

5   $$\phi_{(\alpha,\rho)} = \arccos\left(\hat{\boldsymbol{n}}_\alpha \cdot \hat{\alpha\rho}\right) = \arccos\left(\hat{\boldsymbol{n}}_\alpha \cdot \frac{\hat{\alpha\rho}}{|\hat{\alpha\rho}|}\right).$$

6

7   **Optimal cell normal vectors**

8   No other energy terms will depend on the cell normal vectors $\{\hat{\boldsymbol{n}}_\alpha\}$, so we ask now what the

9   optimal normal vector for a cell is. Suppose a cell is at position $\boldsymbol{r}_\alpha$ with collar vertices at $\boldsymbol{r}_\rho$

10 for $\rho \in \alpha$. We can determine how the cell orients in order to minimise the collar energy with

11 respect to $\hat{\boldsymbol{n}}_\alpha$.

12   For fixed α, the cell orientation vector $\hat{\boldsymbol{n}}_\alpha$ is constrained to have unit length. Hence, we

13 solve the constrained optimisation of $\mathscr{E}_\phi$ by solving the Lagrange multiplier problem with

14 multiplier λ

15 $$0 = \frac{\partial\left[\mathscr{E}_\phi\lambda\left(|\hat{\boldsymbol{n}}_\alpha|^2 - 1\right)\right]}{\partial\hat{\boldsymbol{n}}_\alpha} \tag{3.4}$$

16 $$0 = \frac{\partial\left[\mathscr{E}_\phi + \lambda\left(|\hat{\boldsymbol{n}}_\alpha|^2 - 1\right)\right]}{\partial\lambda}. \tag{3.5}$$

17

18 Using the constraint (solution to equation (3.5)) $|\hat{\boldsymbol{n}}_\alpha|^2 = 1$, we solve

19 $$\lambda\hat{\boldsymbol{n}}_\alpha = 2\sum_{\rho\in\alpha}\left[\arccos\left(\hat{\alpha\rho}\cdot\hat{\boldsymbol{n}}_\alpha\right) - \phi_0\right]\frac{-1}{\sqrt{1 - \left(\hat{\alpha\rho}\cdot\hat{\boldsymbol{n}}_\alpha\right)^2}}\hat{\alpha\rho}$$

20 $$\lambda = 2\left|\sum_{\rho\in\alpha}\left[\arccos\left(\hat{\alpha\rho}\cdot\hat{n}_\alpha\right) - \phi_0\right]\frac{1}{\sqrt{1 - \left(\hat{\alpha\rho}\cdot\hat{n}_\alpha\right)^2}}\hat{\alpha\rho}\right|.$$

21

22 Then the optimal normal vector solves the transcendental equation

$$\hat{\boldsymbol{n}}_\alpha = \frac{\sum_{\rho \in \alpha} \left[\arccos\left(\hat{\alpha\rho} \cdot \hat{\boldsymbol{n}}_\alpha \right) - \phi_0 \right] \frac{-1}{\sqrt{1 - (\hat{\alpha\rho} \cdot \hat{\boldsymbol{n}}_\alpha)^2}} \hat{\alpha\rho}}{\sum_{\rho \in \alpha} \left[\arccos\left(\hat{\alpha\rho} \cdot \hat{\boldsymbol{n}}_\alpha \right) - \phi_0 \right] \frac{1}{\sqrt{1 - (\hat{\alpha\rho} \cdot \hat{\boldsymbol{n}}_\alpha)^2}} \hat{\alpha\rho}} \tag{3.6}$$

Clearly the cell normal vectors must be computed numerically whenever a cell is interacting with several other cells simultaneously in complicated geometries. We can choose to either approximate the normal vectors with a physically reasonable approximation or treat the normal vectors as free arguments to the energy function to be optimised. I discuss both options below.

Approximating cell normal vectors

There are several options for approximating a cell normal vector $\hat{\boldsymbol{n}}_\alpha$ based on positions $\boldsymbol{r}_\alpha$ and $\{\boldsymbol{r}_\rho\}_{\rho \in \alpha}$. The simplest option we might be able to think of is to let $\hat{\boldsymbol{n}}_\alpha$ be the unit vector in the direction $\sum_{\rho \in \alpha} \hat{\alpha\rho}$. This approach has the benefit that collar vertices farther from $\boldsymbol{r}_\alpha$ are weighted more in the cell normal vector, agreeing with the intuition that a more distant collar interaction demands more cell rotation to accommodate it. However, we find that this approach results in unreasonable cell normal vectors for boundary cells as defined in $\mathfrak{G}$ since boundary cells do not have a full ring of boundary collar vertices. For this approach to work, $\mathfrak{G}$ would need to include several more collar vertices which do not describe interactions between cells and add unnecessary complexity. In application, I found that the boundary cell effect of this choice of $\hat{\boldsymbol{n}}_\alpha(\boldsymbol{r}_\alpha, \{\boldsymbol{r}_\rho\}_{\rho \in \alpha})$ substantially affected boundary collar vertex positions after energy equilibration and the overall energy landscape as a function of equilibrium angles ϕ_0, ψ_0.

When initialising a flat sheet, the above averaging approach also does not agree with intuition, since it results in boundary cell normal vectors that do not point in the same direction as normal vectors for cells not on the sheet boundary (figure 3.3). Instead, when a sheet lies flat in the xy-plane, it is expected that all vectors $\hat{\boldsymbol{n}}_\alpha$ point in the $+\hat{z}$ direction provided that collars are above cells in $\boldsymbol{z}$. A viable alternative is to define $\hat{\boldsymbol{n}}_\alpha$ by taking a plane approximation to cell α's collar vertices. The normal vector to this plane oriented away from the cell defines a normal vector that agrees with intuition and supports calculating normals for a non-coplanar set of collar vertices.

The plane approximation approach is easiest achieved using ordinary least squares. Briefly, we approximate $\hat{r}_{\rho 3} = (r_{\rho 1}, r_{\rho 2}) \cdot (\beta_1, \beta_2) + \beta_0$ and minimise the sum of squared

residuals $\sum_{\rho \in \alpha}(\hat{r}_{\rho 3} - r_{\rho 3})^2$ with respect to $\beta_0, \beta_1, \beta_2$. The normal vector of the plane approximation is then $(\beta_1, \beta_2, -1)$ up to normalisation and multiplication by -1.[5]

3.2.2 Cell-cell junction angle ψ energy

As in chapter 2, we aim to produce sheet curvature with the angle ψ that two cells' collars make at their interface. As in section 3.1.3, we calculate the angle between planes defined by two cells α, β and their mutual flanking collar vertices ρ, σ with

$$\psi_{(\alpha,\beta:\rho,\sigma)} = \frac{\pi}{2} - \frac{1}{2} \arccos\left(\hat{\boldsymbol{n}}_{\rho\alpha\sigma} \cdot \hat{\boldsymbol{n}}_{\rho\beta\sigma}\right) \tag{3.7}$$

The normal vectors $\hat{\boldsymbol{n}}_{\rho\alpha\sigma}$ for a plane given by points ρ, α, σ must have a systematically defined orientation, as they can point in either direction $\pm(\boldsymbol{r}_\rho - \boldsymbol{r}_\alpha) \times (\boldsymbol{r}_\sigma - \boldsymbol{r}_\alpha)$. In the geometry used to define ψ in equation (3.7), the collar-cell-collar normal vectors are assumed to be pointing in the direction of the cells' flagella. With the simplifying assumption that the cell normal always points in the inside of the collar, we have that the collar-cell-collar normals must take orientation to align with their corresponding cell normals. Consequently, we let $\hat{\boldsymbol{n}}'_{\rho\alpha\sigma} = \vec{\alpha\rho} \times \vec{\alpha\sigma}$ and set $\hat{\boldsymbol{n}}_{\rho\alpha\sigma} = \text{sgn}(\hat{\boldsymbol{n}}'_{\rho\alpha\sigma} \cdot \hat{\boldsymbol{n}}_\alpha)\hat{\boldsymbol{n}}'_{\rho\alpha\sigma}$.[6]

Defining $\hat{\boldsymbol{n}}_{\rho\alpha\sigma}$ in this way makes it dependent on the cell normal vectors $\hat{\boldsymbol{n}}_\alpha$. However, when minimising the energy, I work to develop methods such that $\text{sgn}(\hat{\boldsymbol{n}}_{\rho\alpha\sigma} \cdot \hat{\boldsymbol{n}}_\alpha)$ remains constant. This corresponds to ensuring that no collar vertices cross through each other (corresponding to microvilli crossing over each other) and that the cell normal vectors remain pointing inside the collars. Hence, I effectively treat the effect of $\hat{\boldsymbol{n}}_\alpha$ on a collar-cell-collar normal vector $\hat{\boldsymbol{n}}_{\rho\alpha\sigma}$ to be constant.

With a common equilibrium collar-collar interface angle ψ_0 (as all cells are assumed equal in their mechanical properties), we express the energy $\mathscr{E}_\psi$

$$\mathscr{E}_\psi = k_\psi \sum_{(\alpha,\beta:\rho,\sigma)} \left(\psi_{(\alpha,\beta:\rho,\sigma)} - \psi_0\right)^2. \tag{3.8}$$

---

[5]The notation here is chosen to be consistent with that typically used in ordinary least squares, hence the hatted values indicate an approximation rather than vector normalisation as I use otherwise.

[6]Here sgn is the sign operator.

3.2.3   Collar length

To provide sufficient flexibility to sheets through collar microvilli, I introduce an energy term $\mathscr{E}_{sp}$ defined by

$$\mathscr{E}_{sp} = k_{sp} \sum_{(\alpha,\rho)} \left| \vec{\alpha\rho} - \ell_{0\alpha\rho} \right|^2, \tag{3.9}$$

where $\ell_{0\alpha\rho}$ is an equilibrium length for edge (α,ρ). The sum indicates summation over all cell, collar pairs (α,ρ) in the sheet $\mathfrak{G}$.

All cells are assumed to take identical properties, so all values $\ell_{0\alpha\rho}$ are set to a constant ℓ_0 unless indicated otherwise. When done so, we find that ℓ_0 is the only length defined in the problem.

When interested in sheets with constrained collar length, we may either take a numerical approach or exploit the above energy term by setting k_{sp} to a large value. The former is discussed in section 3.5.2.

3.3   Minimising sheet energy

ak2351: resume from here

We now have an energy $\mathscr{E}\{r_v\}_{v\in\mathfrak{G}} = \mathscr{E}_\phi + \mathscr{E}_\psi$ which is parameterised over the cell and collar boundary vertex positions. Notably, we treat the topology of the network as fixed, so the indices of the summations for $\mathscr{E}_\phi$ and $\mathscr{E}_\psi$ are unchanged even as we minimise energy.

Flat sheet as a solution

Notice that we have a pair (ϕ_0, ψ_0) that gives $\mathscr{E} = \mathscr{E}_\phi + \mathscr{E}_\psi = 0$. Since the ϕ and ψ energies are nonnegative, the flat sheet is a stable minimum.

Constant collar length constraint

For now, we are numerically constraining the cell-collar lengths at ℓ, their initial lengths (which are constant for all cells). If we want to use the generalisability of our model to use an random initial cell distribution and generate the irregular boundaries with Voronoi tesselation, we will have to relax this condition and add a collar length spring energy to $\mathscr{E}$. The constant

collar length constraint only applies to sheets generated by regular lattices when laid flat on a plane.

The constraint is defined by a vector function $f((c,b)) = |\boldsymbol{r}_c - \boldsymbol{r}_b| - \ell = 0$ for all cell-collar edges (c,b). If n_{collars} is the number of cell-collar edges in {cell-collar edges (c,b)}, then f defines a n_{collars}-vector function.

My optimisation routine requires that we calculate a Jacobian matrix for the vector constraint function. This gets ugly if we use f as written above, but it is fortunately equivalent to set the constraint $f'((c,b)) = |\boldsymbol{r}_c - \boldsymbol{r}_b|^2 - \ell^2 = 0$. It is an interesting problem to take the gradient of $\boldsymbol{f'}$ with respect to all of the coordinates, but I won't include it here. It's implemented in my code.

Solving sheet shape

Numerical optimisation: sensitivity issues and initial conditions

Derive the gradient

Describe how to compute the gradient in an efficient way

3.3.1   Graph topology

For hexagonal lattice start, we

Call back to section 2.1

3.4   Energy gradient descent

Due to the instability of the numerical optimisation routine used above, I moved to minimising the total energy $\mathscr{E}$ explicitly using gradient descent. The goal in taking this approach is to explicitly calculate the gradients $\partial\mathscr{E}/\partial\boldsymbol{r}_\gamma$ of the energy with respect to all coordinate vectors $\boldsymbol{r}_\gamma$ and incrementally take small steps in the reverse direction.

Although gradient descent in several contexts is criticised for being slow and by nature prone to be trapped in local minima, in the context of modeling *C. flexa* sheets it is preferable to a black box optimisation routine. Calculating the gradient analytically amounts to calculating the forces on all coordinates, and taking incremental steps in the direction of the negative gradient amounts to forward integrating Newton's laws $F_\gamma = -\partial\mathscr{E}/\partial\boldsymbol{r}_\gamma$. Consequently, we gain access to the dynamics induced by the simplified model that I describe above. Moreover, the susceptibility of this approach to be trapped in local minima is ideal not only from

an energetic perspective, but also from a numerical one: by taking incremental steps in a

direction known to decrease the energy, any increases indicate a flaw and

ak2351: and what??

In contrast to a numerical optimisation routine, gradient descent requires substantial

explicit calculation. Moreover, the algorithm requires tuning in the step size and relative

decrease in energy tolerance at which to decide the algorithm has terminated.

3.4.1   Deriving the gradient

The linearity of the gradient permits us to take the gradient term-by-term in **??**. For an energy

function $\mathscr{E}(\{\boldsymbol{r}_\gamma\})$ with cell normal vectors $\hat{\boldsymbol{n}}_\alpha$ approximated in terms of each cell's collar

vertices, we find that the gradient $\partial \mathscr{E}_\phi / \partial \boldsymbol{r}_\gamma$ is given by

$$phieq \tag{3.10}$$

ak2351: describe how this can be simplified as a matrix mult problem

As discussed in 3.2.2, an angle $\psi_{(\alpha,\beta:\rho,\sigma)}$ for a cell-cell interface depends in a piecewise

constant way on the cells' normal vectors. While the angles are consequentially only

piecewise differentiable, gradient descent makes reasonable the assumption that there will

not be any discontinuities in $\mathscr{E}_\psi$ for sufficiently small steps in the direction of the negative

gradient. The below expression for $\partial \mathscr{E}_\psi / \partial \boldsymbol{r}_\gamma$ assumes that the sign of $\hat{\boldsymbol{n}}_\alpha \cdot (\vec{\alpha\rho} \times \vec{\alpha\sigma})$

remains constant.

$$\frac{\partial \mathscr{E}_\psi}{\partial \boldsymbol{r}_\gamma} = \sum_{(\alpha,\beta:\rho,\sigma)} \frac{\left(\psi_{(\alpha,\beta:\rho,\sigma)} - \psi_0\right)}{2\sqrt{1 - (\hat{\boldsymbol{n}}_{\rho\alpha\sigma} \cdot \hat{\boldsymbol{n}}_{\rho\beta\sigma})^2}} \left(\hat{\boldsymbol{n}}_{\rho\alpha\sigma} \cdot \frac{\partial \hat{\boldsymbol{n}}_{\rho\beta\sigma}}{\partial \boldsymbol{r}_\gamma} + \hat{\boldsymbol{n}}_{\rho\beta\sigma} \cdot \frac{\partial \hat{\boldsymbol{n}}_{\rho\alpha\sigma}}{\partial \boldsymbol{r}_\gamma}\right)$$

$$\hat{\boldsymbol{n}}_{\rho\alpha\sigma} \cdot \frac{\partial \hat{\boldsymbol{n}}_{\rho\beta\sigma}}{\partial \boldsymbol{r}_\gamma} = \frac{\text{sgn}\left(\vec{\beta\rho} \times \vec{\beta\sigma} \cdot \hat{\boldsymbol{n}}_\beta\right)}{|\vec{\beta\rho} \times \vec{\beta\sigma}|} \left[\left(\frac{\hat{\boldsymbol{n}}_{\rho\alpha\sigma} \cdot \vec{\beta\rho} \times \vec{\beta\sigma}}{|\vec{\beta\rho} \times \vec{\beta\sigma}|^2} \vec{\beta\rho} \times \vec{\beta\sigma} - \hat{\boldsymbol{n}}_{\rho\alpha\sigma}\right) \times \left((\delta_{\gamma\rho} - \delta_{\gamma\beta})\vec{\beta\sigma} - (\delta_{\gamma\sigma} - \right.\right.$$

$$\tag{3.11}$$

The gradient $\partial \mathscr{E}_{\text{sp}} / \partial \boldsymbol{r}_\gamma$ is given by the linear spring force

$$springeq \tag{3.12}$$

Fig. 3.4 todo

3.4.2   Forward integration

Integrating the gradient given by equations equations (3.10) to (3.12) produces the dynamics of sheet bending as in figure 3.4.

> ak2351: discuss the equilbrium states

$$\boldsymbol{r}_\gamma(t+\Delta t) = \boldsymbol{r}_\gamma(t) - \Delta t\, \frac{\partial \mathscr{E}}{\partial \boldsymbol{r}_\gamma}. \tag{3.13}$$

When treating the normal vectors $\hat{\boldsymbol{n}}_\alpha$ as free variables, we must solve modify our force equilibration algorithm to maintain the constraint that $|\hat{\boldsymbol{n}}_\alpha|^2 = 1$. An intuitive option is to step in the direction of the negative gradient and normalise the intermediate vectors at each step:

$$\boldsymbol{n}_\alpha(t+\Delta t) = \hat{\boldsymbol{n}}_\alpha(t) - \Delta t\, \frac{\partial \mathscr{E}}{\partial \hat{\boldsymbol{n}}_\alpha} \tag{3.14}$$

$$\hat{\boldsymbol{n}}_\alpha(t+\Delta t) = \frac{\boldsymbol{n}_\alpha(t+\Delta t)}{\boldsymbol{n}_\alpha(t+\Delta t)}. \tag{3.15}$$

Equivalently, since for a sufficiently small step size the nearest point on the constraint set $|\hat{\boldsymbol{n}}_\alpha|^2 = 1$ to $\boldsymbol{n}_\alpha(t+\Delta t)$ is unique, we may re-express equation (3.15) with $\hat{\boldsymbol{n}}_\alpha(t+\Delta t) = \arg\min_{|\hat{\boldsymbol{n}}_\alpha|^2=1} |\hat{\boldsymbol{n}}_\alpha - \boldsymbol{n}_\alpha(t+\Delta t)|$. Expressed in this way, we see that the update for $\hat{\boldsymbol{n}}_\alpha$ expressed in equations (3.14) and (3.15) is exactly the projected gradient descent algorithm and we expect it to converge [11]. Since the normal component of $\partial \mathscr{E}/\partial \hat{\boldsymbol{n}}_\alpha$ to the constraint set $|bhn_\alpha|^2 = 1$ at step t does not affect $\hat{\boldsymbol{n}}_\alpha(t+\Delta t)$, we can interpret equations (3.14) and (3.15) as taking a step in the direction of the tangent space to the constraint set that reduces $\mathscr{E}$ the most.

> ak2351: discuss the dynamics

While the forward integration works well for small sheets with simple graph topologies, I found that some equilbrium angles ϕ_0, ψ_0 caused the sheet to strain to such an extreme that collar vertices would cross through each other. The resulting increase in energy comes from the discontinuous sign function in the definition of ψ (equation (3.7)), and collar vertices cross over each other due to too large of a step size Δt. While adaptively decreasing the step
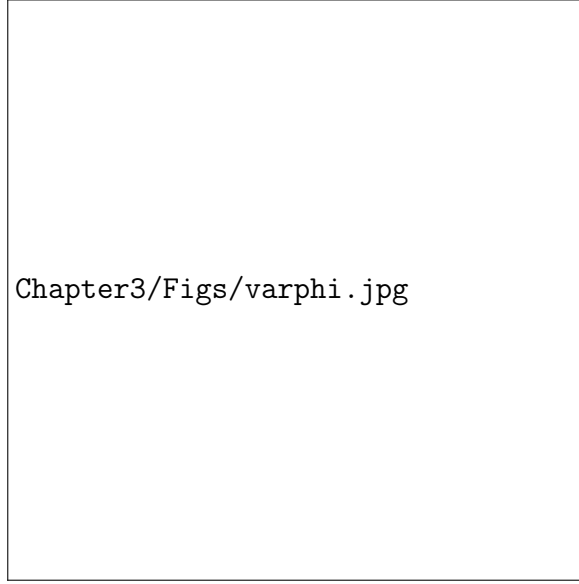
Fig. 3.5 Geometry for calculating $\varphi_{\rho\alpha\sigma}$.

size is a viable option, it would substantially slow the equilibration algorithm. Instead, I introduced an additional term to the energy $\mathscr{E}_\varphi$ based on the angles $\varphi_{\rho\alpha\sigma}$ formed by each cell α and its adjacent pairs of collar vertices ρ, σ when projected onto the plane defined by the cell normal $\hat{\boldsymbol{n}}_\alpha$ (figure 3.5):

$$\mathscr{E}_\varphi = k_\varphi \sum_{(\alpha,\beta:\rho\sigma)} \left(\varphi_{\rho\alpha\sigma} - \varphi_{0\rho\alpha\sigma}\right)^2, \tag{3.16}$$

where $\varphi_{0\rho\alpha\sigma}$ is an equilibrium projected collar-cell-collar angle for each triple. Each angle $\varphi_{0\rho\alpha\sigma}$ is set to the actual value that is evaluated at the initial sheet geometry. Unless specified otherwise, the constant k_φ is set to $0.01k_\phi$.

The angles $\varphi_{\rho\alpha\sigma}$ are calculated similarly to ϕ, ψ (**??** and equation (3.7),

$$\varphi_{\rho\alpha\sigma} = \arccos\left[\vec{\alpha\rho}_\parallel \cdot \vec{\alpha\sigma}_\parallel\right], \tag{3.17}$$

where $\vec{\alpha\rho}_\parallel$ is the projection of $\vec{\alpha\rho}$ onto the plane defined by normal $\hat{\boldsymbol{n}}_\alpha$ and position $\boldsymbol{r}_\alpha$.

> ak2351: give formula for $\vec{\alpha\rho}_\parallel$

The gradient of $\mathscr{E}_\varphi$ is given by

$$varphieq \tag{3.18}$$

3.4.3   Exploring the energy landscape

With the ability to study discrete sheet equilibrium geometries and dynamics, we are prepared to evaluate a mechanism for *C. flexa* folding and inversion. Based on the two collar angle states observed in Brunet et al. [6], a reasonable model would be to assume relaxed-state equilibrium angles $\phi_{\text{in}}, \psi_{\text{in}}$ and a different set of active-state angles $\phi_{\text{out}}, \psi_{\text{out}}$ with instantaneous transition between the two states. The rapid change in individual cell behavior and expected gradual sheet shape change expected from opposing cell-cell interactions align with our expectations from observations Brunet et al. [6].

Although we cannot access true values for the equilibrium angles, modeling *C. flexa* sheets numerically provides the opportunity to explore the entire energy landscape. For sheets generated with a regular hexagonal lattice, we observe the expected diagonal valley where energy in minimised in the energy landscape since the sheet is expected to be flat along those pairs (ϕ_0, ψ_0) (figure 3.6). Substantial sheet deformation and bending is evidently not sufficient to overcome the change in terms in the energy function. The increases in energy when the equilibrium angles are most disparate can be interpreted as collar microvilli stretching or compressing to accommodate sheet bending or a difference in the bending at each cell from the preferred state. For example, cells at neither the centre nor boundary in a bent sheet (figure 3.6, bottom-right or top-left) must contribute a positive contribution to $\mathscr{E}$ since they do not have the symmetric bending at all collar microvilli prescribed by equations (3.3), (3.8) and (3.9).

For graph topologies generated with an icosphere, we observe a more rich energy landscape (**??**). Again we observe a similar minimum energy well running along a diagonal, though the energy increases at the ends since the network of cell-cell connections is not able to accommodate stretching and compression as readily as a sheet generated from a lattice. Notably, the energy well for flagella-out sheets occurs in the region of high ϕ and low ψ. As predicted by equation (2.8), $\phi > \psi$ results in a preferred curvature corresponding to a flagella-out sheet, in agreement with the observed energies. Similarly, we see at these extremely disparate equilibrium angles that the edge of the flagella-in sheet begins to curve outward. The fact that the equilibrium sheet demonstrates this stress indicates that inversion is constrained as a result of cell-cell connections and the collar stiffness k_{sp}.
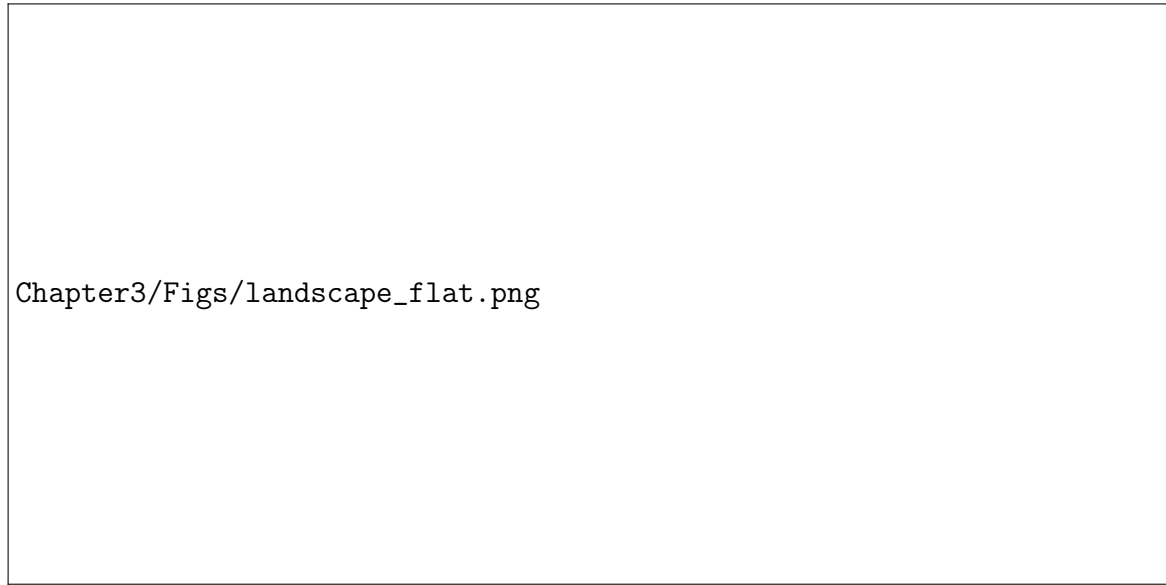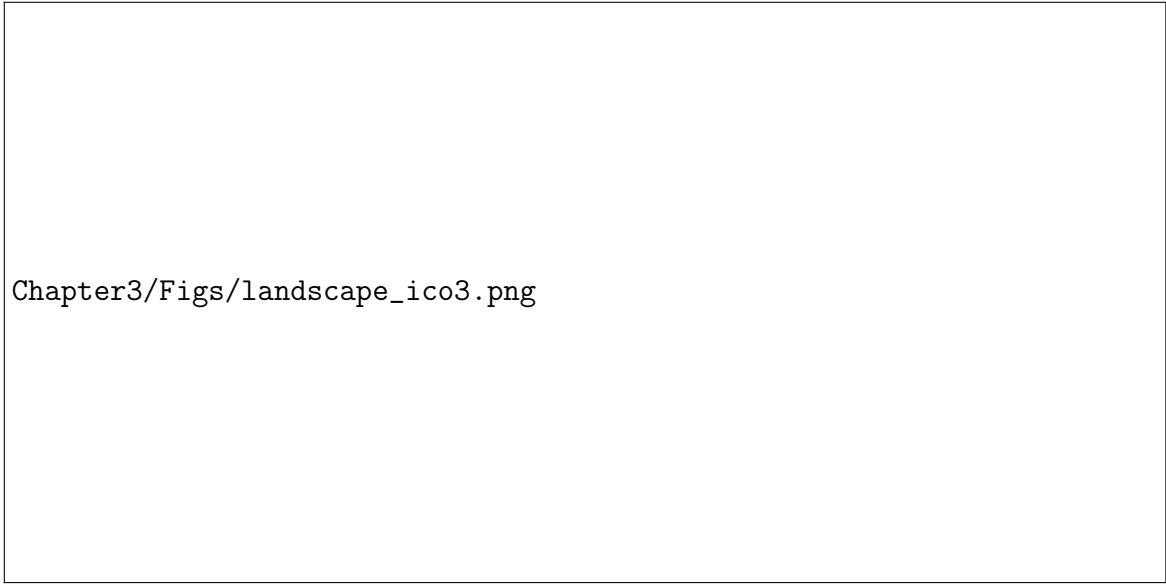
Fig. 3.6 Energy landcsape of a discrete *C. flexa* sheet generated from a hexagonal lattice. Sheets displayed at the right correspond to the corners of the landscape indicated with white crosses.

For low ψ and increasing ϕ in figure 3.7a, there appear to be sudden jumps in the energy profile. When investigated, it emerges that these jumps are the result of buckling at the sheet edges, where an increase in ϕ prompts boundary cells that wrap inward (figure 3.7a, bottom left) to push each other outward.

> ak2351: get ico to invert for small sheets
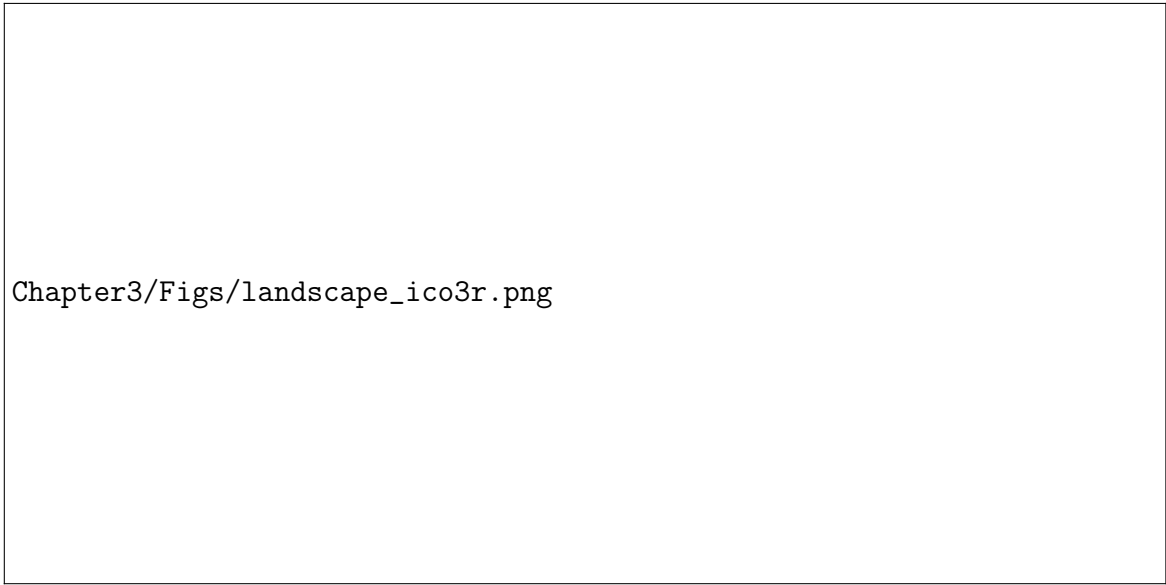
As we are interested in the bistability and transition in *C. flexa* sheets, we are concerned with the global energy minima for both flagella-in and -out sheets. In figure 3.8, the minimum energy orientations throughout the landscape of figure 3.7 are shown. As expected, the lowest possible energy can be achieved in the flagella-in orientation, consistent with the belief that cells are relaxed in this state [6]. With an increase in ϕ_0 and decrease in ψ_0, corresponding to constriction in the apical myosin ring and flaring out or stiffening of the collar, the flagella-in state is preferred.

Based on figure 3.8, we are equipped with a reasonable prediction to describe the inversion dynamics of *C. flexa* sheets. A flagella-in sheet at rest with equilibrium angles ϕ_{in}, ψ_{in} within the energy well of figure 3.7a that immediately changes equilibrium angles to ϕ_{out}, ψ_{out} may be constrained from inverting due to its collar-collar adhesions. Despite this, the equilibrium angles are fixed as a result of environmental conditions and molecular action within the cells, and inversion relaxes the sheet to decrease energy into the higher yet still energetically preferable well of figure 3.7b.
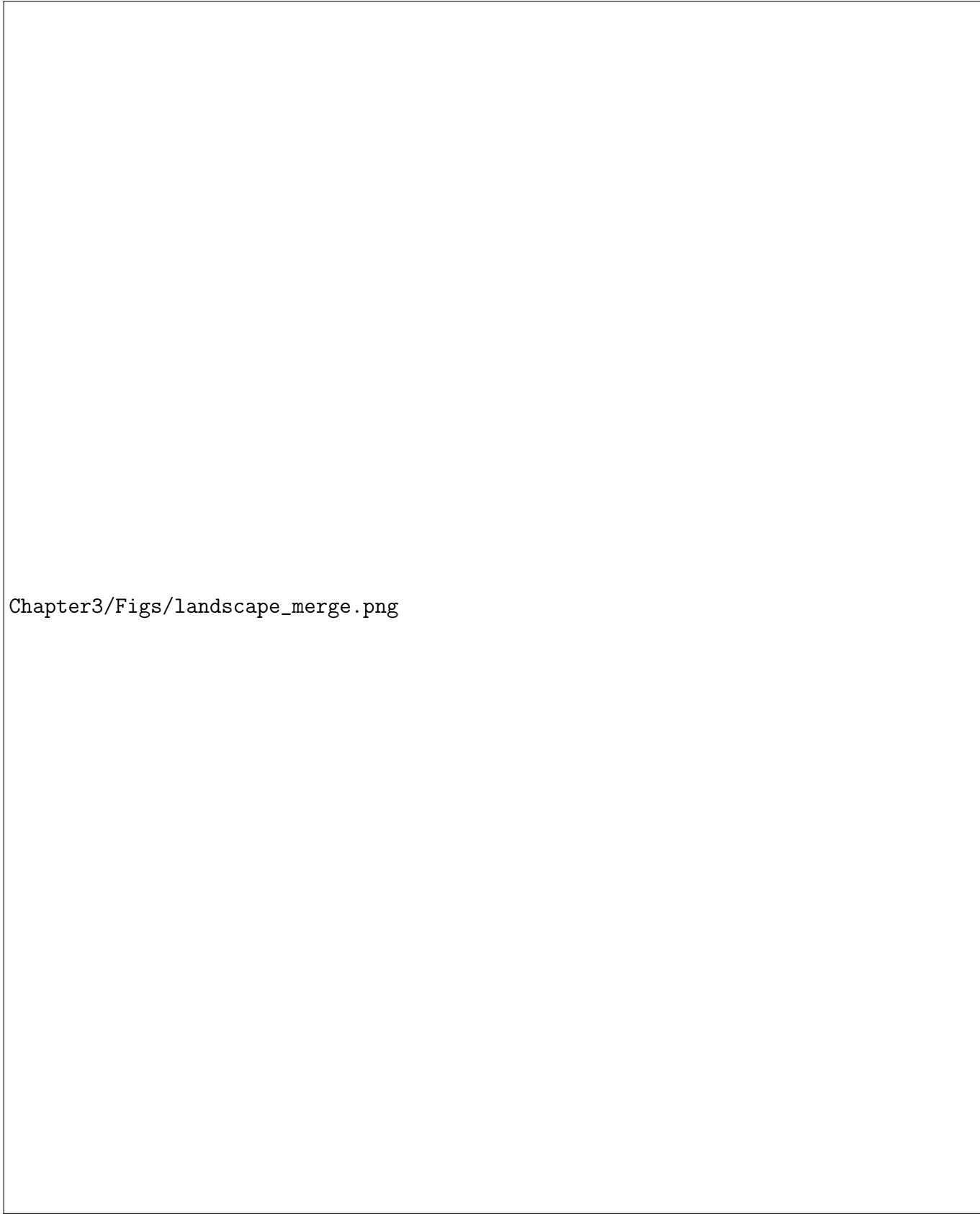
Chapter3/Figs/landscape_ico3.png

(a)

Chapter3/Figs/landscape_ico3r.png

(b)

Fig. 3.7 Energy landscapes for (3.7a) flagella-in and (3.7b) flagella-out sheets of *C. flexa*. The color scaling is the same in both images. The landscapes for a smaller segment of the icosphere were qualitatively similar.

Fig. 3.8 Minimum energies the two landscapes shown in figure 3.7. Values pulled from
figure 3.7a are denoted with red dots and figure 3.7b with orange dots.

1   Despite the favorability of the flagella-out orientation in the active state, it is clear that
2 there is a substantial energetic barrier to reach that state induced by collar-collar adhesion
3 forces and collar stiffness. There is no evidence to suggest changing collar properties, so we
4 are led to predict that changing cell sheet topology is the factor which enables inversion.

> ak2351: collars might break some of their adhesion along their length but not all the way since
> they seem to be connected along the big length

5

6
$$\vec{F}_\gamma = \frac{\partial E}{\partial \vec{r}_\gamma} = 2 \sum_{(\alpha,\rho)} \left(\phi_{(\alpha,\rho)} - \phi_0 \right) \frac{\partial \phi_{(\alpha,\rho)}}{\partial \vec{r}_\gamma} + 2 \sum_{(\alpha,\beta:\sigma,\rho)} \left(\psi(\hat{\bm{n}}_{\sigma\alpha\rho}, \hat{\bm{n}}_{\sigma\beta\rho}) - \psi_0 \right) \frac{\partial \psi_{(\alpha,\beta:\sigma,\rho)}}{\partial \vec{r}_\gamma}$$

7
$$\frac{\partial \phi_{(\alpha,\rho)}}{\partial r_{\gamma i}} = \frac{-1}{\sqrt{1 - (\hat{\bm{n}}_\alpha \cdot (\hat{\alpha\rho}))^2}} \left(\frac{\partial \hat{\bm{n}}_{\alpha j}}{\partial r_{\gamma i}} (\hat{\alpha\rho})_j + \frac{\partial (\hat{\alpha\rho})_j}{\partial r_{\gamma i}} \hat{\bm{n}}_{\alpha j} \right)$$

8
$$\frac{\partial (\hat{\alpha\rho})_j}{\partial r_{\gamma i}} = \frac{(\delta_{\gamma\rho} - \delta_{\gamma\alpha})}{|r_\rho - r_\alpha|} \left(\delta_{ij} + (\hat{\alpha\rho})_i (\hat{\alpha\rho})_j \right)$$

9
$$\frac{\partial \hat{\bm{n}}_{\alpha j}}{\partial r_{\gamma i}} = \frac{\mathbb{1}_{\gamma \in \text{collars}(\alpha)} - n\delta_{\gamma\alpha}}{|\sum_{(\alpha,\rho)} (r_\rho - r_\alpha)|} \left(\delta_{ij} - \hat{\bm{n}}_{\alpha i} \hat{\bm{n}}_{\alpha j} \right)$$

10
$$\frac{\partial \psi_{(\alpha,\beta:\sigma,\rho)}}{\partial r_{\gamma i}} = \frac{-1}{\sqrt{1 - (\hat{\bm{n}}_{\rho\alpha\sigma} \cdot \hat{\bm{n}}_{\rho\beta\sigma})^2}} \left(\frac{\partial \hat{\bm{n}}_{\rho\alpha\sigma j}}{\partial r_{\gamma i}} \hat{\bm{n}}_{\rho\beta\sigma j} + \frac{\partial \hat{\bm{n}}_{\rho\beta\sigma j}}{\partial r_{\gamma i}} \hat{\bm{n}}_{\rho\alpha\sigma j} \right)$$

11
$$\frac{\partial \hat{\bm{n}}_{\rho\alpha\sigma j}}{\partial r_{\gamma i}} = \text{too big see notes}$$
12

3.5   Including both cells and collar boundaries

3.5.1   Initial sheet

3.5.2   Numerical optimisation routine

16 Finally, we numerically optimise. I changed ϕ_0 to be defined relative to the initial value of
17 ϕ, and likewise for ψ. If we make ϕ_0 smaller and ψ_0 larger, we expect the cell collars to
18 contract and for cell-cell distances to lengthen. In other words, we expect the sheet to curve
19 upward, so that the cells on the edges go in the direction that the collars are.
20   The numerical optimisation problem gives a clean sensible solution, which is shown
21 projected onto the *xy*-plane in Figure 3.9. We can tell that the sheet is curved just looking at
22 this alone, which is a massive relief and confirmation of what we expect.

Fig. 3.9 Figure in the same style of Figure 3.3 showing the cell sheet projected onto the *xy*-plane after minimising energy.

¹ The solution in Figure 3.9 is for $\phi_0 = 0.99\phi_{\text{init}}$ and $\phi_0 = 1.03\psi_{\text{init}}$, where ϕ_{init} and ψ_{init}
² are the initial angles in the flat sheet state. We could now bask in the glory of our solution
³ and look at it in 3d (Figure 3.10a).
⁴ The resulting structure is really pretty sensitive to small changes in ϕ_0, ψ_0. Figure 3.10b
⁵ shows the structure that comes out of $\phi_0 = 0.9\phi_{\text{init}}, \psi_0 = 1.15\psi_{\text{init}}$.

Chapter3/Figs/shallow.png

(a)

Chapter3/Figs/deep.png

(b) 3d projections of the curved sheet formed by $\phi_0 = 0.9\phi_{\text{init}}, \psi_0 = 1.15\psi_{\text{init}}$.

Fig. 3.10 Cell sheet geometry from the hexagonal lattice in Figure 3.3 and parameters
(3.10a) $\phi_0 = 0.99\phi_{\text{init}}, \phi_0 = 1.03\psi_{\text{init}}, \ell_0 = \ell_{\text{init}} = 1.52$, (3.10b) $\phi_0 = 0.9\phi_{\text{init}}, \psi_0 = 1.15\psi_{\text{init}}$,
$\ell_0 = \ell_{\text{init}} = 1.52$.

3.5.3   Topology

In section 3.3, I mentioned that the flat sheet is a stable minimum. But it is here because the lattice is regular. A single pentagon in a hexagonal lattice (like a football (soccer) ball, thanks Lloyd) will make it so no ϕ_0 and ψ_0 will make every cell make the other cells flat.

What I think is interesting about this is the connection between graph topology and surface geometry. I think, in a continuous sense, graph topology affects Gaussian curvature through the energy function.

Adding noise to initial cell positions in Figure 3.3

We expect the initial lattice in Figure 3.3 to produce a sheet with 6-fold symmetry. Since the graph of connections is produced by a Voronoi tessellation, small changes to initial boundary cell positions can change the graph topology for boundary cells.

When adding noise to the initial cell positions, the change in topology at some boundary nodes results in substantial effects felt over the sheet. Figure 3.11 shows the effect of different topology at the boundary.
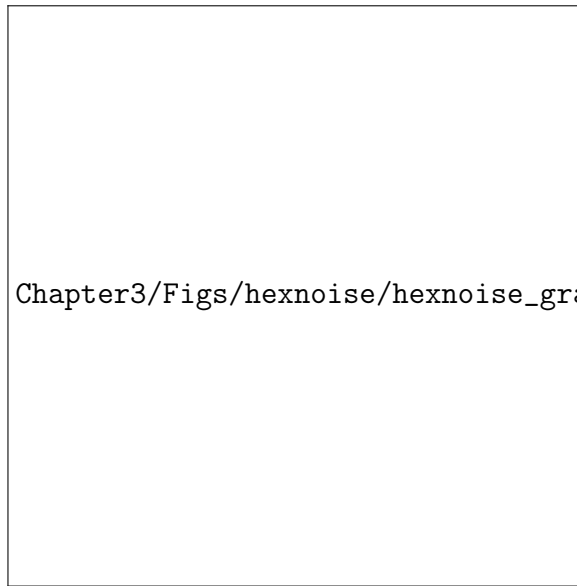
Interior cell topology

We can also add or merge nodes in a regular lattice (Figure 3.3) to introduce nodes with irregular degree. There are more complex ways of making different graph topologies (like Lloyd's initial icosphere) but I don't have curved initial conditions or more complicated lattices implemented yet.

Figure 3.12 shows a sheet with cell of degree 7 (7 bordering cells) and 3.13 shows a sheet with two neighboring cells of degree 5.

3.5.4   Larger cell sheets

If if inverting a sheet of cells involves flattening it out at the edges, then a small sheet will be able to do this easier than a large one. This is because the cells on the outside have to stretch their collars less if the sheet is smaller when they flatten out.

Chapter3/Figs/hexnoise/hexnoise_graph.png

(a) Initial lattice drawn as in Figure 3.3.

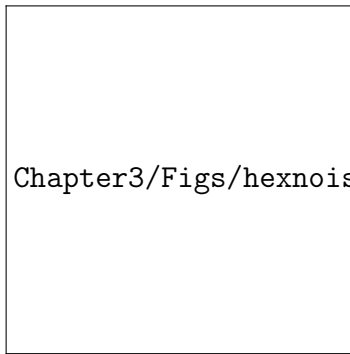Chapter3/Figs/hexnoise/hexnoise0.8_0.8_1.52_10_graph.png Chapter3/Figs/hexnoise/hexnoise0.8_0.8_1.52_10_plot.png

(b) Sheet shape when $\phi_0 = 0.8$, $\psi_0 = 0.8$, $\ell_0 = 1.52$.

Chapter3/Figs/hexnoise/hexnoise0.95_0.8_1.52_10_graph.png Chapter3/Figs/hexnoise/hexnoise0.95_0.8_1.52_10_plot.png
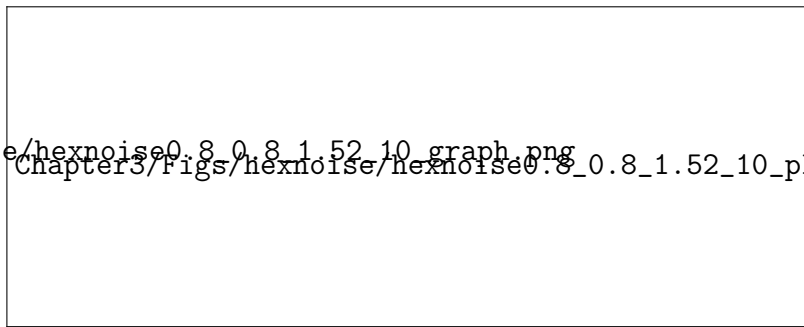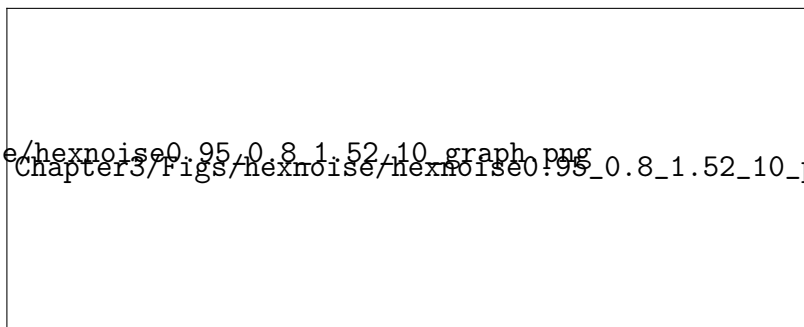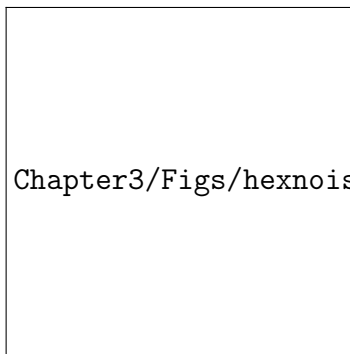
(c) Sheet shape when $\phi_0 = 0.95$, $\psi_0 = 0.8$, $\ell_0 = 1.52$.

Fig. 3.11 Cell sheet geometry with noise added to the initial lattice. The graph topology is affected at the sheet boundary (subfigure 3.11a) from the Voronoi tesselation. This minor change has substantial effects on the sheet geometry (subfigures 3.11b, 3.11c).
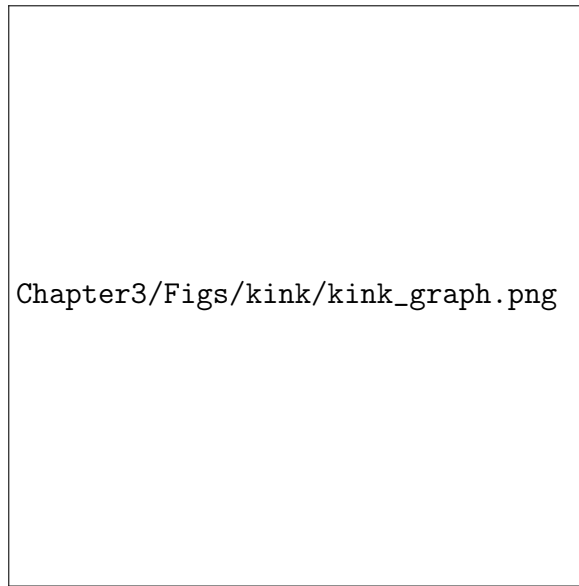
Chapter3/Figs/kink/kink_graph.png

(a) Initial lattice drawn as in Figure 3.3.

Chapter3/Figs/kink/kink0.8_0.8_1.52_10_graph.png

Chapter3/Figs/kink/kink0.8_0.8_1.52_10_plot.png

(b) Sheet shape when $\phi_0 = 0.8$, $\psi_0 = 0.8$, $\ell_0 = 1.52$.

Chapter3/Figs/kink/kink0.95_0.8_1.52_10_graph.png

Chapter3/Figs/kink/kink0.95_0.8_1.52_10_plot.png
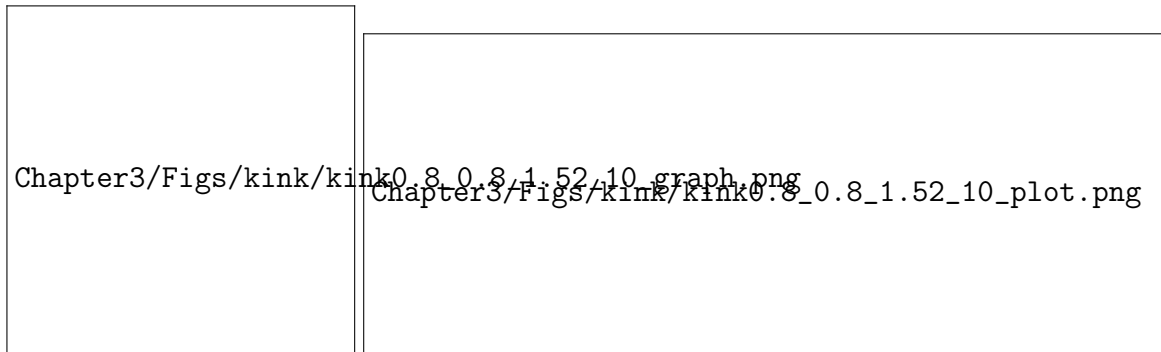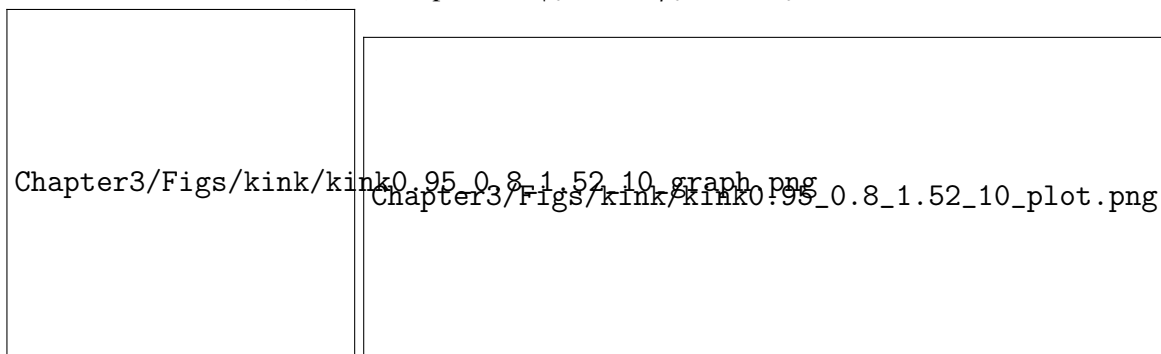
(c) Sheet shape when $\phi_0 = 0.95$, $\psi_0 = 0.8$, $\ell_0 = 1.52$.

Fig. 3.12 Cell sheet geometry with a node of degree 7. The graph topology is affected in the sheet interior (subfigure 3.12a). This minor change has substantial effects on the sheet geometry (subfigures 3.12b, 3.12c).
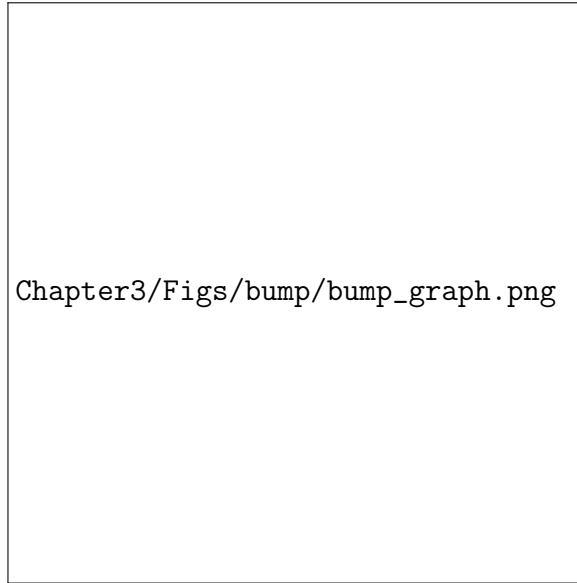
Chapter3/Figs/bump/bump_graph.png

(a) Initial lattice drawn as in Figure 3.3.

Chapter3/Figs/bump/bump0.8_0.8_1.52_10_graph.png   Chapter3/Figs/bump/bump0.8_0.8_1.52_10_plot.png

(b) Sheet shape when $\phi_0 = 0.8$, $\psi_0 = 0.8$, $\ell_0 = 1.52$.

Chapter3/Figs/bump/bump0.95_0.8_1.52_10_graph.png   Chapter3/Figs/bump/bump0.95_0.8_1.52_10_plot.png
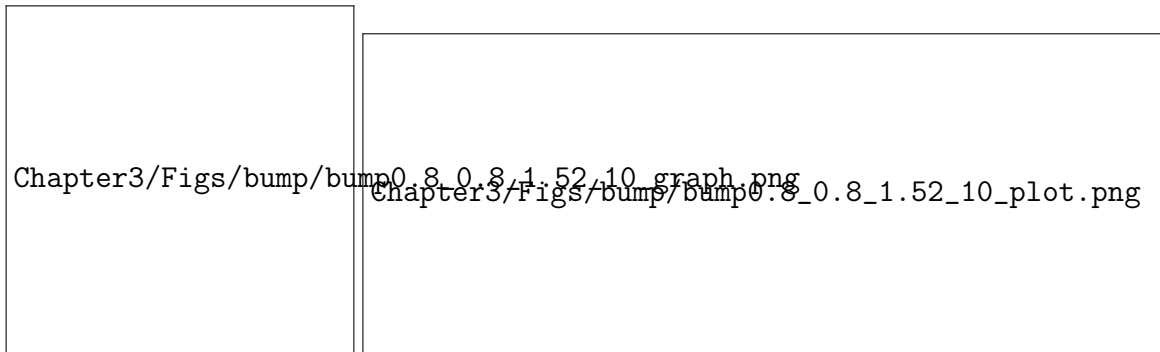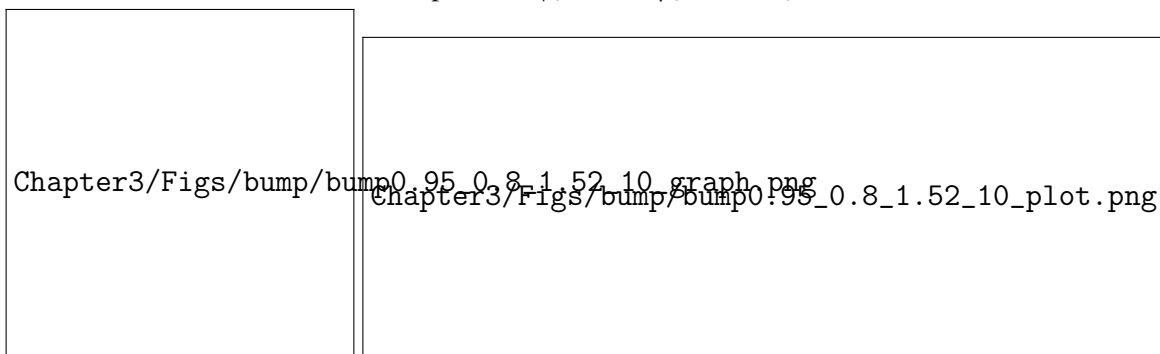
(c) Sheet shape when $\phi_0 = 0.95$, $\psi_0 = 0.8$, $\ell_0 = 1.52$.

Fig. 3.13 Cell sheet geometry with a node of degree 7. The graph topology is affected in the sheet interior (subfigure 3.13a). This minor change has substantial effects on the sheet geometry (subfigures 3.13b, 3.13c).
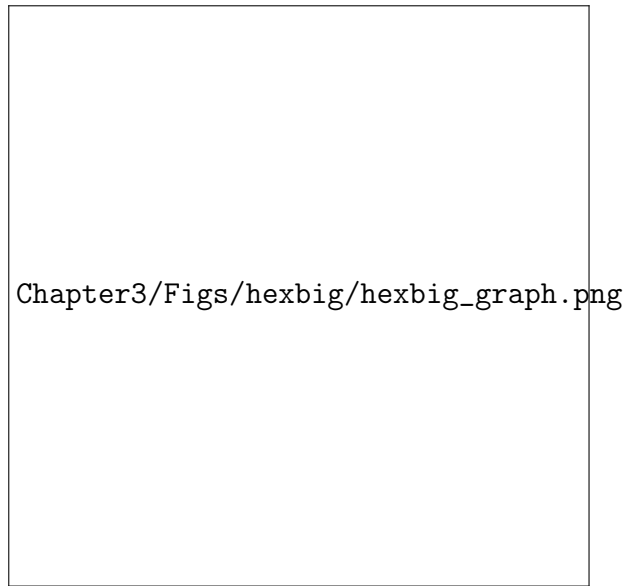
Chapter3/Figs/hexbig/hexbig_graph.png

(a) Initial lattice drawn as in Figure 3.3.

Chapter3/Figs/hexbig/hexbig0.8_0.8_1.35_10_graph.png Chapter3/Figs/hexbig/hexbig0.8_0.8_1.35_10_plot.png

(b) Sheet shape when $\phi_0 = 0.8$, $\psi_0 = 0.8$, $\ell_0 = 1.52$.

Chapter3/Figs/hexbig/hexbig0.95_0.8_1.35_10_graph.png Chapter3/Figs/hexbig/hexbig0.95_0.8_1.35_10_plot.png
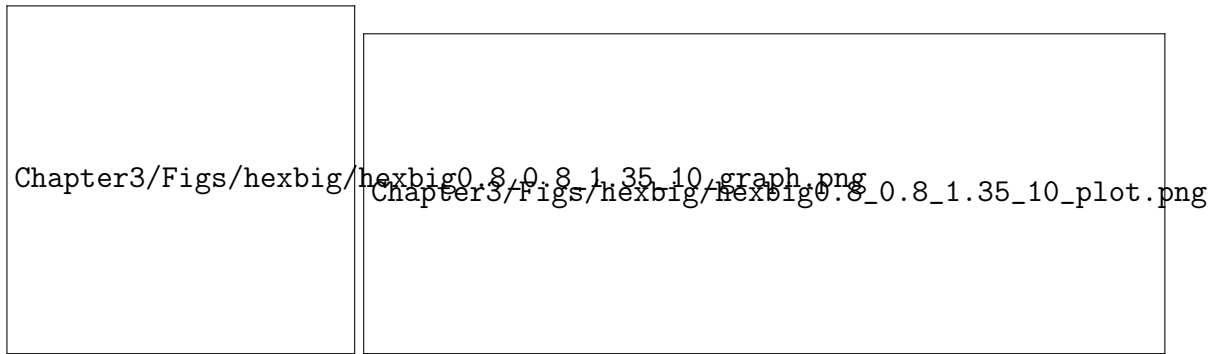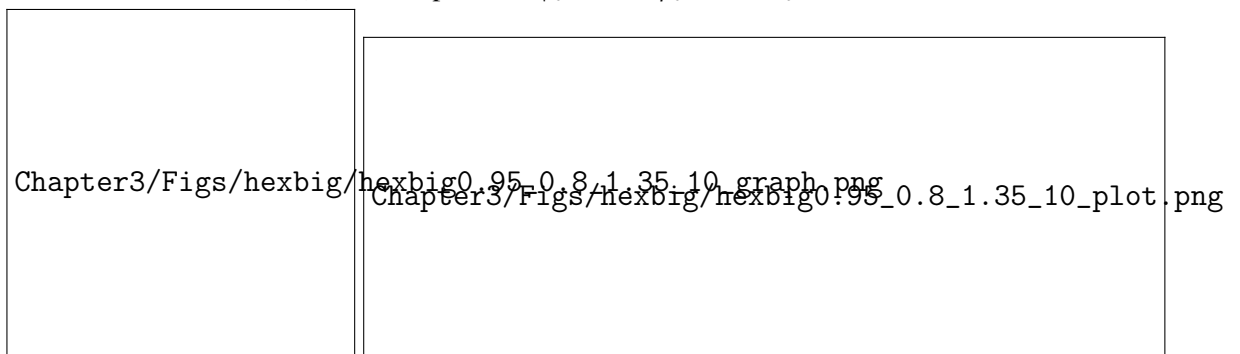
(c) Sheet shape when $\phi_0 = 0.95$, $\psi_0 = 0.8$, $\ell_0 = 1.52$.

Fig. 3.14 Cell sheet geometry with a node of degree 7. The graph topology is affected in the sheet interior (subfigure 3.14a). This minor change has substantial effects on the sheet geometry (subfigures 3.14b, 3.14c).

Chapter 4

Discussion

4.1   section

Think about why *C. flexa* has the behavior that it does. Given how other choanoflagellates like *S. rosetta* get their morphology by division [13, 21], it could be that *C. flexa* forms by division and has evolved its contractile ring to take advantage of that. This would make sense from the perspective that choanoflagellate cells aligned and lined up next to each other drive the strongest flows (though still not stronger than they could individually) Kirkegaard and Goldstein [18]. This paper also found that being farther from a wall increases flux. This is interesting considering that the feeding state of *C. flexa* was observed to be so ineffective at swimming that it sank and remained in place. However this was on a slide and in the absense of external flows Brunet et al. [6].

When thinking about *C. flexa* in the context of multicellularity, we should not overlook the simplicity by which it achieves large-scale geometric changes. While we can develop increasingly complex models by introducing collar filament bending, tension and stress at the collar filaments' bases, or the effects of the contractile ring, my work demonstrates that a coarse description of individual cells is sufficient to explain the behavior that we observe in colonies. Compare this with *Volvox*, which uses connections and communication between cells to control its inversion. One might imagine that the complexity of a molecular pathway for a single cell to exhibit phototaxis or regulate feeding/swimming efficiency could easily exceed the ring contraction as currently understood in *C. flexa* [6].

ak2351: cite Volvox inversion papers, cite papers on phototaxis or swimming signalling pathways

4.2   Discrete cell sheet topology

The discrete model of *C. flexa* demonstrates that deviations from a hexagonally packed sheet at as few as one cell are sufficient to induce substantial bending. The geometric effects of such *topological defects* are established in the context of crystal structures.

As discussed in the comparison between the continuous and discrete model, a topological defect at a cell can be likened to a different preferred Gaussian curvature in the continuous perspective. Indeed, Seung and Nelson [30] wrote a comparable model with defected lattices that deformed to an energy function given by stretching energies and bending energies. There, the authors also found that

References

[1] Alegado, R. A., Brown, L. W., Cao, S., Dermenjian, R. K., Zuzow, R., Fairclough, S. R., Clardy, J., and King, N. (2012). A bacterial sulfonolipid triggers multicellular development in the closest living relatives of animals. *elife*, 1.

[2] Asadzadeh, S. S., Larsen, P. S., Riisgård, H. U., and Walther, J. H. (2019). Hydrodynamics of the leucon sponge pump. *Journal of the Royal Society Interface*, 16(150):20180630.

[3] Berg, H. C. and Purcell, E. M. (1977). Physics of chemoreception. *Biophysical journal*, 20(2):193–219.

[4] Boraas, M. E., Seale, D. B., and Boxhorn, J. E. (1998). Phagotrophy by a flagellate selects for colonial prey: a possible origin of multicellularity. *Evolutionary Ecology*, 12(2):153–164.

[5] Brunet, T. (2022). personal communication.

[6] Brunet, T., Larson, B. T., Linden, T. A., Vermeij, M. J., McDonald, K., and King, N. (2019). Light-regulated collective contractility in a multicellular choanoflagellate. *Science*, 366(6463):326–334.

[7] Caroli, M., de Castro, P. M., Loriot, S., Rouiller, O., Teillaud, M., and Wormser, C. (2010). Robust and efficient delaunay triangulations of points on or close to a sphere. In *International Symposium on Experimental Algorithms*, pages 462–473. Springer.

[8] Carr, M., Leadbeater, B. S., Hassan, R., Nelson, M., and Baldauf, S. L. (2008). Molecular phylogeny of choanoflagellates, the sister group to metazoa. *Proceedings of the National Academy of Sciences*, 105(43):16641–16646.

[9] Dayel, M. J., Alegado, R. A., Fairclough, S. R., Levin, T. C., Nichols, S. A., McDonald, K., and King, N. (2011). Cell differentiation and morphogenesis in the colony-forming choanoflagellate salpingoeca rosetta. *Developmental biology*, 357(1):73–82.

[10] De Saedeleer, H. (1930). Recherches sur les choanocytes; l'origine des spongiaires. *Annales de la Sociétié royale zoologique de Belgique*, pages 16–21.

[11] Eicke, B. (1992). Iteration methods for convexly constrained ill-posed problems in hilbert space. *Numerical Functional Analysis and Optimization*, 13(5-6):413–429.

[12] Ellis, W. N. (1930). Recent researches on the choanoflagellata (craspedomonadines) (freshwater and marine) with description of new genera and species. *Annales de la Société royale zoologique de Belgique*, 60:49–88.

[13] Fairclough, S. R., Dayel, M. J., and King, N. (2010). Multicellular development in a choanoflagellate. *Current Biology*, 20(20):R875–R876.

[14] Goldstein, R. E. (2015). Green algae as model organisms for biological fluid dynamics. *Annual review of fluid mechanics*, 47:343.

[15] Herron, M. D. and Michod, R. E. (2008). Evolution of complexity in the volvocine algae: transitions in individuality through darwin's eye. *Evolution: International Journal of Organic Evolution*, 62(2):436–451.

[16] James-Clark, H. (1871). Note on the infusoria flagellata and the spongiae ciliatae. *Journal of Natural History*, 7(39):247–248.

[17] King, N. (2004). The unicellular ancestry of animal development. *Developmental cell*, 7(3):313–325.

[18] Kirkegaard, J. B. and Goldstein, R. E. (2016). Filter-feeding, near-field flows, and the morphologies of colonial choanoflagellates. *Physical Review E*, 94(5):052401.

[19] Landau, L. D., Lifšic, E. M., Lifshitz, E. M., Kosevich, A. M., and Pitaevskii, L. P. (1986). *Theory of elasticity: volume 7*, volume 7. Elsevier.

[20] Lang, B., O'kelly, C., Nerad, T., Gray, M., and Burger, G. (2002). The closest unicellular relatives of animals. *Current biology*, 12(20):1773–1778.

[21] Larson, B. T., Ruiz-Herrero, T., Lee, S., Kumar, S., Mahadevan, L., and King, N. (2020). Biophysical principles of choanoflagellate self-organization. *Proceedings of the National Academy of Sciences*, 117(3):1303–1311.

[22] Lauterborn, R. (1898). *Protozoën-Studien: IV. T. Flagellaten aus dem Gebiete des Oberrheins. Aus dem Zoologischen Institut der Universität Heidelberg.(M. 2 Taf.)*. A. Lauterborn.

[23] Leadbeater, B. S. (1977). Observations on the life-history and ultrastructure of the marine choanoflagellate choanoeca perplexa ellis. *Journal of the Marine Biological Association of the United Kingdom*, 57(2):285–301.

[24] Leadbeater, B. S. (1983). Life-history and ultrastructure of a new marine species of proterospongia (choanoflagellida). *Journal of the Marine Biological Association of the United Kingdom*, 63(1):135–160.

[25] Leadbeater, B. S. C. (2008). Choanoflagellate evolution: the morphological perspective. *Protistology*, 5:256–267.

[26] Mah, J. L., Christensen-Dalsgaard, K. K., and Leys, S. P. (2014). Choanoflagellate and choanocyte collar-flagellar systems and the assumption of homology. *Evolution & development*, 16(1):25–37.

[27] Michelin, S. and Lauga, E. (2011). Optimal feeding is optimal swimming for all péclet numbers. *Physics of Fluids*, 23(10):101901.

[28] Powers, T. R. (2010). Dynamics of filaments and membranes in a viscous fluid. *Reviews of Modern Physics*, 82(2):1607.

[29] Sebé-Pedrós, A., Degnan, B. M., and Ruiz-Trillo, I. (2017). The origin of metazoa: a unicellular perspective. *Nature Reviews Genetics*, 18(8):498–512.

[30] Seung, H. S. and Nelson, D. R. (1988). Defects in flexible membranes with crystalline order. *Physical Review A*, 38(2):1005.

[31] Solari, C. A., Ganguly, S., Kessler, J. O., Michod, R. E., and Goldstein, R. E. (2006). Multicellularity and the functional interdependence of motility and molecular transport. *Proceedings of the National Academy of Sciences*, 103(5):1353–1358.

[32] Stanley, S. M. (1973). An ecological theory for the sudden origin of multicellular life in the late precambrian. *Proceedings of the National Academy of Sciences*, 70(5):1486–1489.

[33] Stokes, G. G. et al. (1851). On the effect of the internal friction of fluids on the motion of pendulums. *Transactions of the Cambridge Philosophical Society*.

[34] Tuzet, O. (1963). The phylogeny of sponges according to embryological, histological, and serological data, and their affinities with the protozoa and the cnidaria. *The lower metazoa. Comparative biology and phylogeny*, pages 129–148.

[35] Wiggins, C. H., Riveline, D., Ott, A., and Goldstein, R. E. (1998). Trapping and wiggling: elastohydrodynamics of driven microfilaments. *Biophysical journal*, 74(2):1043–1060.